ACS NANO

Cite This: ACS Nano 2018, 12, 9040–9050

www.acsnano.org

ARTICLE

Breaking the Nanoparticle Loading–Dispersion Dichotomy in Polymer Nanocomposites with the Art of Croissant-Making

Giovanni Santagiuliana,[†] Olivier T. Picot,[†,‡] Maria Crespo,[†] Harshit Porwal,[†,‡] Han Zhang,[†,‡] Yan Li,[†,§] Luca Rubini,[∥] Samuele Colonna,[⊥] Alberto Fina,[⊥] Ettore Barbieri,[†,#] Anne B. Spoelstra,[▽] Giulia Mirabello,[▽] Joseph P. Patterson,[▽] Lorenzo Botto,[†] Nicola M. Pugno,[∥,○,†] Ton Peijs,[†,‡] and Emiliano Bilotti*[,†,‡]

[†]School of Engineering and Materials Science, Queen Mary University of London, Mile End Road, London E1 4NS, United Kingdom

[‡]Nanoforce Technology Limited, Mile End Road, London E1 4NS, United Kingdom

[§]Gemmological Institute, China University of Geosciences, 388 Lumo Road, Wuhan, China 430074

[∥]Laboratory of Bio-inspired & Graphene Nanomechanics, Department of Civil, Environmental and Mechanical Engineering, University of Trento, Via Mesiano 77, 38123 Trento, Italy

[⊥]Dipartimento di Scienza Applicata e Tecnologia, Politecnico di Torino, 15121 Alessandria, Italy

[#]Japan Agency for Marine-Earth Science and Technology, Department of Mathematical Science and Advanced Technology, Yokohama Institute for Earth Sciences, 3173-25, Showa-machi, Kanazawa-ku, Yokohama, Kanagawa 236-0001, Japan

[▽]Laboratory of Materials and Interface Chemistry & Centre for Multiscale Electron Microscopy Department of Chemical Engineering and Chemistry, Eindhoven University of Technology, Eindhoven, The Netherlands

[○]Ket-Lab, Edoardo Amaldi Foundation, Italian Space Agency, Via del Politecnico, 00133 Rome, Italy

Supporting Information

ABSTRACT: **The intrinsic properties of nanomaterials offer promise for technological revolutions in many fields, including transportation, soft robotics, and energy. Unfortunately, the exploitation of such properties in polymer nanocomposites is extremely challenging due to the lack of viable dispersion routes when the filler content is high. We usually face a dichotomy between the degree of nanofiller loading and the degree of dispersion (and, thus, performance) because dispersion quality decreases with loading. Here, we demonstrate a potentially scalable pressing-and-folding method (P & F), inspired by the art of croissant-making, to efficiently disperse ultrahigh loadings of nanofillers in polymer matrices. A desired nanofiller dispersion can be achieved simply by selecting a sufficient number of P & F cycles. Because of the fine microstructural control enabled by P & F, mechanical reinforcements close to the theoretical maximum and independent of nanofiller loading (up to 74 vol %) were obtained. We propose a universal model for the P & F dispersion process that is parametrized on an experimentally quantifiable "*D* factor". The model represents a general guideline for the optimization of nanocomposites with enhanced functionalities including sensing, heat management, and energy storage.**

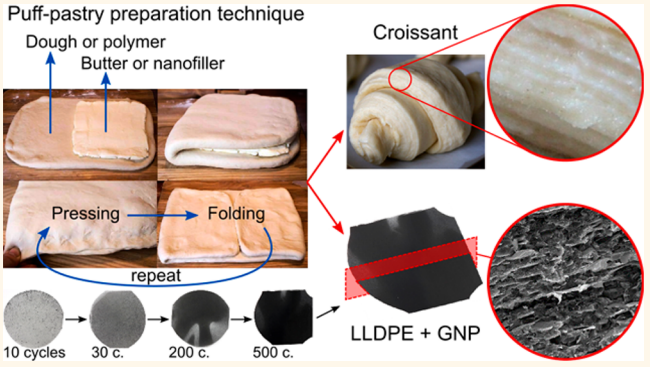

KEYWORDS: *polymer nanocomposites, nanoparticle dispersion, graphene, nanoclay, predictive model, multifunctional materials*

Facing technological challenges in fields such as transportation, soft robotics, biomedical, and wearable electronics will require the availability of materials able to simultaneously bear loads and integrate multiple

Received: April 17, 2018
Accepted: September 4, 2018
Published: September 4, 2018

DOI: 10.1021/acsnano.8b02877
ACS Nano 2018, 12, 9040–9050

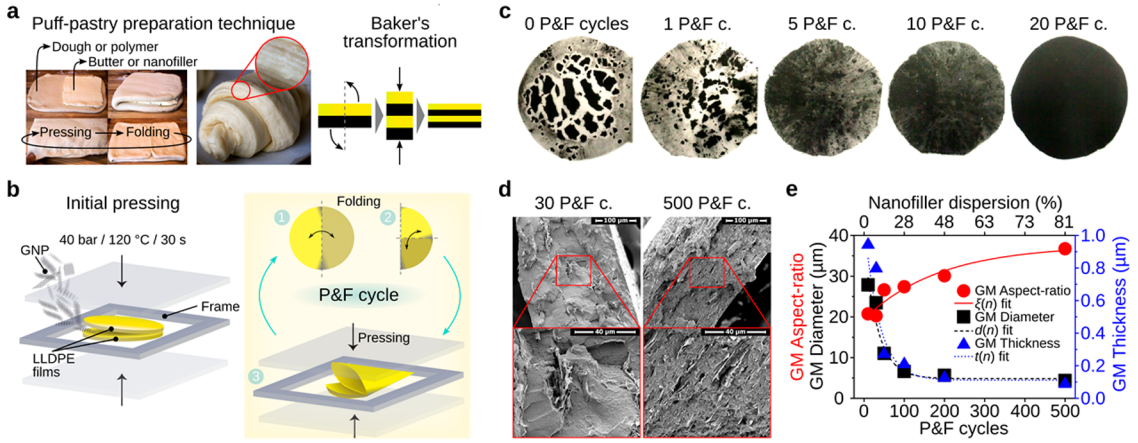

Figure 1. Nanofiller dispersion process. (a) The P & F technique draws inspiration from the puff-pastry preparation technique (left), and its stretching and folding effect can be idealized as a Baker's transformation (right). (b) Schematic of the P & F technique. (c) Top-view images of samples of LLDPE containing 4.8 vol % of graphite nanoplatelets (GNP) after different P & F cycles (sample diameter of ~8 cm and sample thickness of ~300 μm). (d) Cross-sectional SEM images of LLDPE containing 4.8 vol % GNP samples for very different filler dispersion levels: the left image shows thick and well-separated GNP agglomerates, and the right image shows well-dispersed GNPs. (e) Geometric mean (GM) values of diameter, thickness, and aspect ratio (ratio between diameter and thickness) of GNP agglomerates. The GM values were obtained from the analysis of cross-sections of LLDPE containing 4.8 vol % GNP samples for different P & F cycles. The lines are best fits using eq 4.

functionalities such as sensing, adaptation, responsiveness, energy harvesting, and communication.[1] Polymer nanocomposites are promising candidates for meeting these requests because they employ nanoparticles having exceptional intrinsic properties. Graphene,[2] for instance, has been proven to possess exceptional mechanical properties,[3] excellent gas-barrier properties,[4] high charge-carrier mobility and high thermal conductivity,[5,6] and visual transparency.[7] However, it has proven to be difficult to exploit the intrinsic properties of the embedded nanoparticles: the performance of nanocomposites are often disappointing and well below theoretical predictions. For example, according to classical composite theories,[8] we would expect graphene nanocomposites to exhibit extraordinary mechanical performance. However, only a very limited number of papers have reported nanocomposites standing up to these expectations.[9−12] Good performance and agreement with the theory is usually observed for very low nanofiller contents only (below 1 vol %).[8] However, this is the range in which the absolute performance is low, questioning the use of nanoparticles in place of more-conventional alternatives. The issue lies in the following dilemma: the smaller the material's size, the more appealing its intrinsic properties but also the more difficult the control over the nanoparticle dispersion quality during processing.[13,14]

However, nanocomposites are readily found in nature, and their intrinsic performance can surpass that of the best man-made composites. For instance, nacre, often taken as the golden standard in structured composites, combines $CaCO_3$ "bricks" and protein "mortar" in a layered microstructured composite ~3000 times tougher than each of nacre's components.[15] The hierarchical structure of nacre is believed to be the key to its properties. Hence, researchers have attempted to exploit nanoparticle properties by developing methods to obtain better microstructural control. The best resulting nanocomposites have demonstrated high mechanical performances,[9−12] unusual interaction with light,[16,17] resistance to flammability,[18−22] self-regulating heating,[23,24] energy management,[25−27] high electrical and thermal conductivity,[28] and sensing and structural health monitoring.[29−32]

However, the control over nanoparticle dispersion is usually compromised for high filler loading,[11,12,33−37] making it impossible to exploit the desired large nanofiller−polymer interfacial area.[38] As a consequence, nanocomposites often contain nanoparticle agglomerates that dramatically reduce performance[11,12,33,39] unless they were prepared by bottom-up, but hardly scalable, approaches.[40−42]

To overcome the dichotomy between nanofiller loading and dispersion (and, hence, properties), herein we present an iterative materials processing technique (P & F) that draws inspiration from the process of preparation of puff pastry to make croissants (Figure 1a). This technique can create nanocomposites with well-defined nanofiller dispersion levels without the loss of dispersion efficiency, even at ultra-high nanofiller loadings. This is not achievable by traditional solution-mixing or melt-blending techniques. Moreover, we propose an analytical model that quantitatively correlates nanocomposite properties with nanofiller dispersion level. To prove the potential of the P & F technique, we produce nanocomposites with exceptional combination of functionalities, including energy management, self-heating, and strain sensing.

RESULTS AND DISCUSSION

Micromechanical Considerations and Modeling of the P & F Dispersion Process. The P & F technique is based on the addition of nanoparticles (*i.e.*, graphite nanoplatelets, GNP) in between two polymer films (*i.e.*, linear-low density polyethylene, LLDPE; Figure 1b, left), followed by the application of P & F cycles (Figure 1b, right) an arbitrary number of times. Each P & F cycle is composed of a folding step in which an approximately circular GNP-containing layer is folded twice to produce a quadrant slice and a pressing step executed at a temperature slightly above the polymer melting point (≅120°C for LLDPE). The pressing step produces a strong flow that simultaneously breaks down the agglomerates, aligns the dispersed particles, and substantially increases the GNP−LLDPE contact area, yielding a well-mixed dispersion after a number of cycles. The P & F process implements

DOI: 10.1021/acsnano.8b02877
ACS Nano 2018, 12, 9040−9050

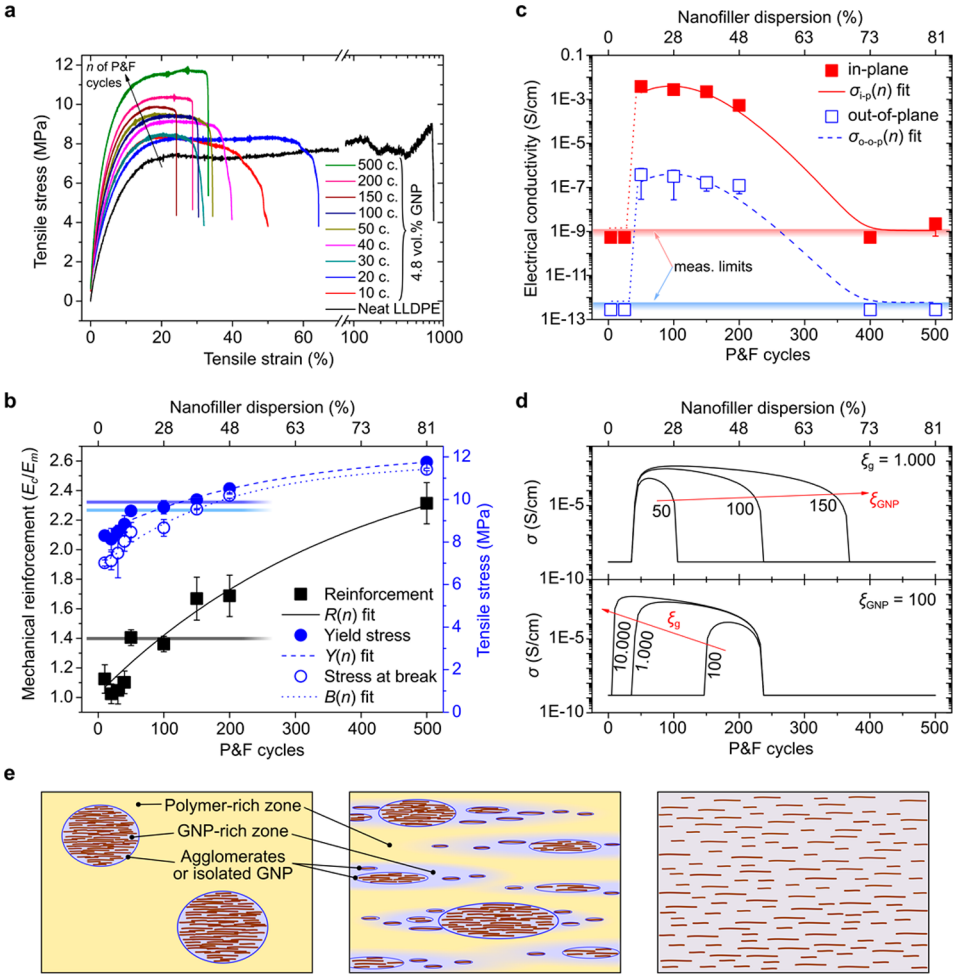

Figure 2. Effect of nanofiller dispersion on mechanical and electrical properties of LLDPE containing 4.8 vol % GNP nanocomposites. (a) Representative stress−strain curves. (b) Measured mechanical reinforcement *R*, stress at yield *Y*, and stress at break *B* with best fits using eq 4.The three horizontal lines represent the yield stress (top line), stress at break, and reinforcement (bottom line) of the reference sample prepared by traditional melt blending. (c) Electrical conductivity as a function of P & F cycles *n* (horizontal shades areas indicates the lower measurement limits for in-plane and out-of-plane electrical conductivities; dotted lines are guides for the eye) fitted with eq 5. The measurement limits are due to the apparatus employed that could measure a minimum conductance of 2×10^{-11} S, multiplied by the geometries of the samples used: $1.5/(0.8 \times 0.03)$ cm^{-1} for in-plane measurements and $0.03/(1 \times 1)$ cm^{-1} for out-of-plane. (d) Theoretical predictions of nanocomposite electrical conductivities based on the model of Wang *et al.*[51] for different GNP aspect-ratios (top graph, assuming that ξ_g reaches the value of 1000 after 500 cycles) and for GNP-rich zones that reach different aspect ratios after 500 P & F cycles (bottom graph). (e) Representation of the nanocomposite microstructures with the polymer-rich and GNP-rich zones.

Baker's transformation[43] (Figure 1a, right) at very high applied viscous stresses.

As shown in Figure 1c, after a few P & F cycles the color of the nanocomposites becomes homogeneous to the naked eye (see also Figure S5). At small cycle numbers, the nanocomposites present large GNP agglomerates (Figure 1d, left). The size of the agglomerates decreases with increasing cycles (Figure 1e), and many well-dispersed individual particles appear throughout the samples, forming a layered structure (see further microstructural observations in section S.7.1 of the Supporting Information). After 500 P & F cycles, the initial agglomerates have mostly disappeared (Figure 1d, right), and the thickness of the dispersed particles approaches that of individual GNP (~30 nm, see section S.3 of the Supporting Information for GNP characterizations).

The combined effect of dispersion and orientation obtained by P & F cannot be reached by conventional melt processing like twin-screw melt-compounding or multilayer co-extrusion[44] (which is also based on the Baker's transformation). The flow has a dominant extensional component that orients the particles with their flat faces perpendicular to the pressing direction. The squeeze flow in the thin gap between the plates produces large shear rates. Such high shear rates may not be achievable by conventional multilayer co-extrusion because the materials are processed at temperatures much higher than the polymer melting point, otherwise they will hardly flow through the extrusion line. By solving the velocity profile for a power-law fluid using the lubrication approximation, we estimate the volume-averaged shear rate magnitude during each P & F cycle to be between $\dot{\gamma} = 12\ s^{-1}$ and $\dot{\gamma} = 1150\ s^{-1}$ in the final stages of compression, depending on whether the polymer is assumed to slip freely from the wall or to adhere perfectly to it. Given the high viscosity of the polymer (we are working just above the melting temperature), the corresponding viscous stresses are large, between 3 kPa and 90 kPa (assuming 4.8 vol %; see section S.11.1 of the Supporting Information), and sufficient to break down the initial aggregates (from the surface energy of graphene $\Gamma \cong 70$ mN/m and the diameter of the platelets D_p,

DOI: 10.1021/acsnano.8b02877
ACS Nano 2018, 12, 9040−9050

we estimate the yield strength $\sigma_y \propto \frac{\Gamma}{D_p}$ of the initial aggregates to be smaller than 0.74 kPa; see section S.11.1 of the Supporting Information). The controlled flow in P & F has a further crucial benefit. With conventional processing methods, characterized by complex flow streamlines, the flow can promote re-agglomeration rather than dispersion if converging streamlines are present that force the particles to come into contact with each other. In contrast, in the P & F approach, the dominant extensional flow increases the particle separation at each cycle by "stretching" the fluid containing the suspended platelets.

A key aspect of the method is that after the pressing step has ended, the shear rate goes practically to zero. As a consequence, the sample viscosity increases dramatically, "freezing" the microstructure (for samples at 120 °C containing 4.8 vol % GNP, the viscosity increases from $\eta \cong 10\,\text{Pa·s}$ for $\dot{\gamma} \cong 10\,\text{s}^{-1}$ to $\eta \cong 10^5\,\text{Pa·s}$ for $\dot{\gamma} \cong 10^{-3}\,\text{s}^{-1}$). Moreover, the sample is cooled and folded at room temperature. Hence, once dispersed, the platelets remain dispersed until the next pressing step. To quantify the dispersion during the P & F process, we can define a dispersion factor D as:

$$D \equiv \frac{A(n)}{A_p} \tag{1}$$

where $A(n)$ and A_p are the nanofiller–matrix contact area at cycle n and the total nanofiller surface area, respectively. The D factor ranges from 0 for completely agglomerated GNPs to 1 for perfectly dispersed GNPs. This parameter can either be measured indirectly [*e.g.*, by analyzing scanning electron microscopy and transmission electron microscopy (SEM and TEM, respectively) images][39] or analytically derived *a priori* from the preparation technique used (see section S.11.3 of the Supporting information for melt-blending and section S.11.4 of the Supporting Information for solution mixing and casting).

By assuming that the variation of D within a Δn interval depends on a distribution rate I (a constant that describes how fast the polymer melt erodes the agglomerates and distributes the nanoparticles) and on a saturation term $A_p - A(n)$ (once all of the GNPs are in contact with LLDPE, D becomes 1 and cannot further increase; see section S.11.2 of the Supporting Information), we can estimate that D changes with n according to:

$$D(n) = 1 - \frac{(A_p - A_0)}{A_p} e^{-I \times n} \tag{2}$$

where A_0 is the initial contact area. We calculate a pre-exponential factor $(A_p - A_0)/A_p$ of 0.999 by analyzing the optical pictures of the samples at the first few cycles and a distribution rate $I \approx 3.3 \times 10^{-3}$ using two different methods (sections S.11.5 and S.11.6 of the Supporting Information): one based on the analysis of the optical pictures of films prepared at low P & F cycles and the other one determined by fitting the mechanical and electrical properties of the nanocomposites presented later. We used eq 2 to convert the number of P & F cycles into a nanofiller dispersion level on the top axis of Figures 1e and 2b,c. The knowledge of the dispersion state allows the prediction of nanocomposite physical properties.

Prediction of Nanocomposite Properties for Different Dispersion Levels. Nanocomposite physical properties can be parametrized on D assuming that the effective nanofiller loading V_p^{eff} scales with the nominal nanofiller loading V_p in the same way as the area does:

$$V_p^{\text{eff}}(D) \equiv D \times V_p \tag{3}$$

The effective volume fraction can be used to replace V_p inside theoretical models for composites (such as the Halpin–Tsai model[45,46] for the elastic modulus or the Pukanszky model[47] for the yield stress), provided that the nanofiller dispersion level is known, or to back-calculate an unknown D factor. Any physical properties P that follows the rule-of-mixture,[48,49] such as the Young's modulus or the thermal conductivity, can be expressed (see section S.11.2 of the Supporting Information) as:

$$P(D) \approx P_0 + (P_{\text{th}} - P_0) \times D \tag{4}$$

where P_0 is the value of P for $D = 0$, and P_{th} is the value of P when the nanofiller is perfectly dispersed. In contrast, properties that are very sensitive to percolation, such as the electrical conductivity σ, are expected to follow an exponential relation (section S.11.2 of the Supporting Information):

$$\sigma(D) = \sigma_{\text{th}} + (\sigma_M - \sigma_{\text{th}}) \times e^{-a(D-D_c)^2} \tag{5}$$

where σ_{th} is the theoretical conductivity at high dispersion levels, σ_M is the maximum conductivity reached at a critical nanofiller dispersion level D_c, and a is a parameter that describes how fast the conductivity changes with interparticle distance (and thus with the dispersion level). In the next section, we will explain this correlation between nanofiller dispersion and electrical conductivity in more detail. Despite their simplicity, eqs 4–6 are very useful for both interpreting nanocomposites physical properties and predictions and materials design.

Effect of GNP Dispersion Level on Nanocomposite Properties. Figure 2a shows representative stress–strain curves corresponding to different P & F cycles for samples containing 4.8 vol % GNP. The mechanical reinforcement E_c/E_m (ratio between elastic modulus E_c of the composite and elastic modulus of the matrix, with $E_m = 140 \pm 5$ MPa), the stress at yield Y, and the stress at break B are improved by nanofiller dispersion (Figure 2b), as expected from previous studies.[39,50] Because the yield stress depends also on the nanofiller specific surface area,[38] its increase compared to neat LLDPE (7.85 ± 0.27 MPa) is likely explained by an increasing nanofiller–matrix interfacial area with P & F cycles. However, nanofiller dispersion may change also the crystallinity and the spherulitic and lamellar features of the polymer, which, in turn, can further affect the nanocomposite mechanical properties. In sections S.4 and S.5 of the Supporting Information, we show that these changes are negligible for our samples, so any mechanical improvement must be mainly caused by an increased nanofiller–polymer interface. The stress at break overtakes the value of neat LLDPE (9.5 ± 0.7 MPa) only after 150 P & F cycles; for this number of cycles, the failure of initiation due to stress concentrations generated by GNP agglomerates is overcome (see fracture surfaces in section S.7.2 of the Supporting Information). For comparison, a reference sample containing 4.8 vol % GNP prepared by melt-blending followed by compression-molding presents mechanical properties as low as those of samples prepared between 100 and 150 P & F cycles (Figure 2b and section S.8 of the Supporting

DOI: 10.1021/acsnano.8b02877
ACS Nano 2018, 12, 9040–9050

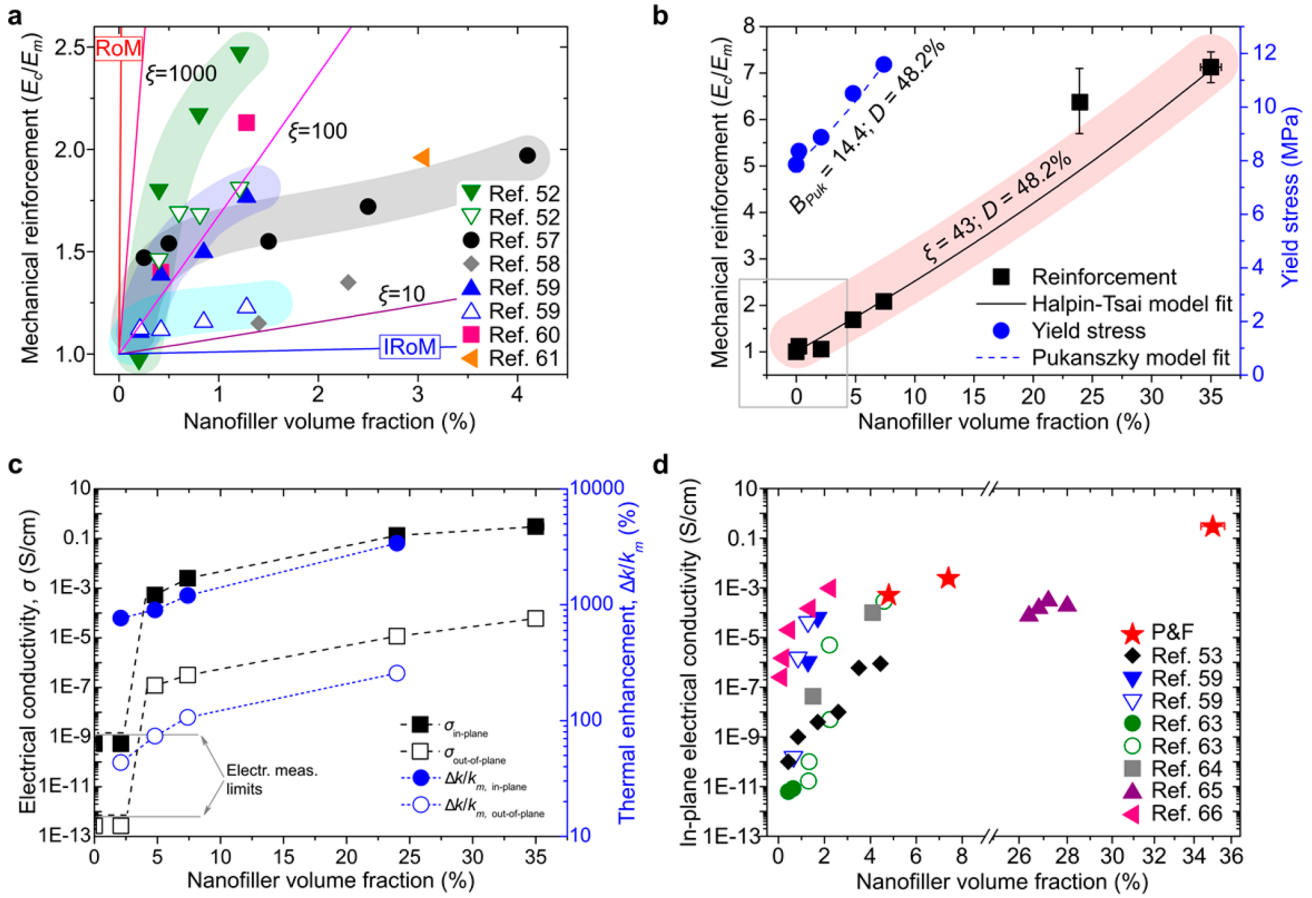

Figure 3. Properties of LLDPE nanocomposites for different GNP loadings but similar dispersion level (48.2%). (a) Mechanical reinforcement of GNP−LLDPE nanocomposites from literature, together with prediction lines of the Halpin−Tsai model at different aspect ratios ξ of monolayer graphene. The shadowed areas are a guide for the eye to highlight the decrease of reinforcing efficiency with nanofiller loading. For some cases, there are two data sets per reference corresponding to nanocomposites prepared by different techniques or with different matrix and nanofiller functionalization. (b) Mechanical reinforcement and yield stress of GNP−LLDPE nanocomposites for *n* = 200 P & F cycles. The frame corresponding to low-volume fractions indicates the region where literature data typically fall (see Figure 3a). Because of the high GNP loading that increases nanocomposite brittleness, the sample containing 35 vol % GNP does not show any yield before fracture. The modified Halpin−Tsai and Pukanszky models modified by eq 3 fit the reinforcement and yield data. In both fits, the *D* factor was kept constant at 48.2% (value found for previous nanocomposites containing 4.8 vol % GNP prepared at *n* = 200). (c) Electrical conductivity of GNP−LLDPE nanocomposites prepared with *n* = 200 (lines are guides for the eye) and thermal conductivity enhancement with respect to the value obtained for LLDPE, k_m. (d) In-plane electrical conductivity of LLDPE−GNP nanocomposites. Note the high in-plane conductivity of 0.3 S/cm for the sample at 35 vol % obtained via P & F.

Information). This is believed to be mainly due to the reduced in-plane alignment of the GNP nanoparticles.

The anisotropic microstructure observed by SEM is reflected in the electrical properties (Figure 2c): the in-plane conductivity is approximately 4 orders of magnitude higher than the out-of-plane conductivity. The in-plane and out-of-plane conductivities of samples prepared with less than 50 P & F cycles are not measurable, suggesting well-isolated GNP agglomerates inside the matrix. Between 50 and 150 P & F cycles, the dispersion of the particles leads to an optimally conductive network, and the conductivities reach a maximum (this rise in conductivity with the nanofiller dispersion agrees with several literature observations).[39,52,53] The conductivities then decrease at higher P & F cycles, suggesting a breakup of the percolating network. This other behavior agrees with the results of Tkalya *et al.*, who reported increased percolation thresholds in nanocomposites with improved graphene dispersions.[54] The reduction in electrical conductivity can also be explained by a partial fragmentation of GNP. This effect, however, should be less dominant than the nanofiller dispersion/distribution effect because there is no evidence of a reduction of mechanical properties with P & F cycles. Notably, a reference sample prepared by melt-blending and compression molding (also containing 4.8 vol % GNP) is not electrically conductive.

To better understand the reasons behind the trend of the electrical conductivities with the P & F cycles, we refer to the study of Wang *et al.*, who developed a conductivity model based on the continuum theory that takes into account the effects of nanofiller agglomeration, imperfect nanofiller−matrix interface, and electron tunnelling.[51] Because of the GNP agglomerates, the volume of nanocomposites must be divided into two different zones: a GNP-rich zone and a polymer-rich zone (Figure 2e). The size of the GNP-rich zones may not be the same of those reported in Figure 1e for the GNP agglomerates: the GNP-rich zones (represented by violet areas in Figure 2e as opposed to the blue contours used to denote the agglomerates and individual GNP that can be measured by SEM) can consists also of well-dispersed GNP that are just well close to each other so that their local concentration is

DOI: 10.1021/acsnano.8b02877
ACS Nano 2018, 12, 9040−9050

higher than V_p. Assuming that the polymer-rich zone does not contain any GNP, the GNP concentration inside the GNP-rich zones is $V_{GNP} = V_p/V_g$,[51] where V_g is the volume fraction of the GNP-rich zones inside the nanocomposites. The value of V_g must increase from V_p at the first few P & F cycles to one at very high cycles, where there is no more distinction between GNP-rich and polymer-rich zones (Figure 2e). Unfortunately, there is no direct way to measure the size of the GNP-rich zones. However, considering that the P & F dispersion mechanism involves repetitive extensional flows, it is reasonable to expect that the GNP-rich zones increase their aspect-ratio ξ_g with the number of P & F cycles. Based on the model of Wang *et al.*,[51] when ξ_g is higher than the aspect ratio ξ_{GNP} of the individual GNP, the overall electrical percolation decreases and the conductivity of the nanocomposites increases. Indeed, approximating their model, the nanocomposite conductivity σ is controlled by the electrical percolation between the GNP-rich zones:

$$\sigma \cong \sigma_g(V_g - V_g^c)^2 \tag{6}$$

where V_g^c is the critical volume fraction of the GNP-rich zones, and σ_g is their conductivity, which is based in turn on the percolation of the GNP within the GNP-rich zones:

$$\sigma_g \cong \sigma_{GNP}(V_{GNP} - V_{GNP}^c)^2 \tag{7}$$

where V_{GNP}^c is the critical volume fraction of the GNP inside the GNP-rich zones. Some literature studies[55,56] suggest that the critical volume fractions are inversely correlated to the filler aspect ratio: $V_g^c \propto 1/\xi_g$ and $V_{GNP}^c \propto 1/\xi_{GNP}$ and, hence, the reason why ξ_g must be higher than ξ_{GNP} to enhance the conductivity of nanocomposites. Using eq 7 inside eq 6, we can simulate the trend of nanocomposite conductivity with P & F cycles (Figure 2d, where we assumed a linear increment of V_g and ξ_g with P & F cycles). This trend is quite similar to that of data in Figure 2c and to the model of eq 5. Therefore, the parameter D_c of eq 5 represents the situation in which there is the best compromise between ξ_g and V_{GNP} during the P & F process that gives the maximum possible conductivity, σ_M: $D_c \propto V_{GNP}/\xi_g$ and $\sigma_M \propto \xi_{GNP}/D_c$.

In summary, our nanocomposites can be divided in three categories according to the nanofiller dispersion state: (1) nanocomposites with $D < 15\%$ containing inhomogeneous GNP distribution and isolated GNP agglomerates that do not form an electrically conductive network and for which the mechanical properties are comparable with or worse than those of the neat LLDPE; (2) nanocomposites with $15\% < D < 50\%$ containing well-dispersed and aligned GNPs, showing high and anisotropic conductivities and good mechanical reinforcement; and (3) nanocomposites with $D > 50\%$ presenting highly dispersed and aligned GNP, having enhanced mechanical properties but poor electrical conductivity. The combination of electrical and mechanical properties is thus a strong function of the parameter D.

Toward Ultrahigh Nanofiller Loadings. Figure 3a compares values found in literature[52,57−61] for the reinforcement of layered nanocomposites of LLDPE and GNP/graphene with theoretical predictions using the Halpin−Tsai model, which assumes "optimally dispersed" systems. None of the literature data sets follow the linear trend expected from the theory: the data sets show the typical reduction in reinforcing efficiency with nanofiller loading, commonly attributed to decreasing nanofiller dispersion quality as the concentration of nanoparticle increases. Here, we examine the properties of nanocomposites prepared at 200 P & F cycles (LLDPE and GNP are not affected by such high cycles, as demonstrated in section S.9 in the Supporting Information) as a function of GNP loading.

We find that the mechanical reinforcement *vs* volume fraction data for P & F (representative stress−strain curves can be found in Figure S10) can be well-fitted by the Halpin−Tsai and Pukanszky models using V_p^{eff} with a fixed value of $D = 48.2\%$ (Figure 3). The model parameters correspond to a nanofiller aspect-ratio of 43 (in agreement with the theoretical one, $\xi_{th} = 38$, from the fit in Figure 1e) and nanofiller−matrix interaction parameter B_{Puk} of 14.4, similar to values reported for clay nanocomposites.[62] Considering that no compatibiliser was used, the high value of the parameter B_{Puk} suggests a fairly good GNP−LLDPE interaction. These results demonstrate that the dispersion efficiency of the P & F technique (and, hence, the resulting reinforcement) does not decrease at high nanofiller loadings (*i.e.*, D factor remains constant), contrary to what is usually reported (Figure 3a).

The in-plane conductivity of our samples is 4 orders of magnitude higher than the out-of-plane conductivity (Figure 3c). This reflects the anisotropic layered microstructure of the nanocomposite. Considering the aspect ratio of our GNP (~40), we should expect a percolation threshold around 15 vol % if GNP were perfectly dispersed.[55] The measured percolation threshold lies between 2.1 and 4.8 vol % (Figure 3c). This range is theoretically expected for perfectly dispersed nanoplatelets with aspect ratios of 150−250. Therefore, the nonhomogeneous, imperfect GNP dispersion ($D \approx 50\%$) in our nanocomposites increases the electrical conductivity (as depicted in Figure 2c), hence lowering the percolation threshold to values theoretically expected for higher aspect-ratio fillers. This result corroborates our conductivity model of eq 5.

The high electrical conductivities come with massive in-plane thermal conductivity enhancements: >10 W/m·K, more than 3000% higher than LLDPE thermal conductivity. The out-of-plane conductivity increases up to ~1 W/m·K. To the best of our knowledge, this is the highest combination of thermal conductivity enhancement and thermal anisotropy ever reported. A comparison of the in-plane electrical conductivity data with the values found in the literature[53,59,63−66] for layered nanocomposites of LLDPE with GNP/graphene (Figure 3d) shows how our samples are the most-conductive nanocomposites reported. It is noted that the conductivity is predicted to be even higher for a D-factor close to $D_c \approx 25\%$.

Material Multifunctional Design and General Applicability of the Approach. The P & F approach addresses the optimization of nanocomposite microstructures to fulfill particular technological applications. For example, a layered microstructure with perfectly dispersed nanoparticles is needed for materials with enhanced mechanical, gas-barrier, or thermal properties, *e.g.*, films for food packaging and flexible electronics[67,68] and heat-dissipating devices.[28] We measured the thermal conductivity of polymer nanocomposites with 4.8 vol % GNP after 400 P & F cycles. Unexpectedly, thermal conductivities were ~3 W/m·K in-plane (~900% higher than neat LLDPE thermal conductivity) and ~0.3 W/m·K out-of-plane while being electrically insulating in all directions (average interparticle distance longer than electron mean free path).[69] The combination of high thermal conductivity and

DOI: 10.1021/acsnano.8b02877
ACS Nano 2018, 12, 9040−9050

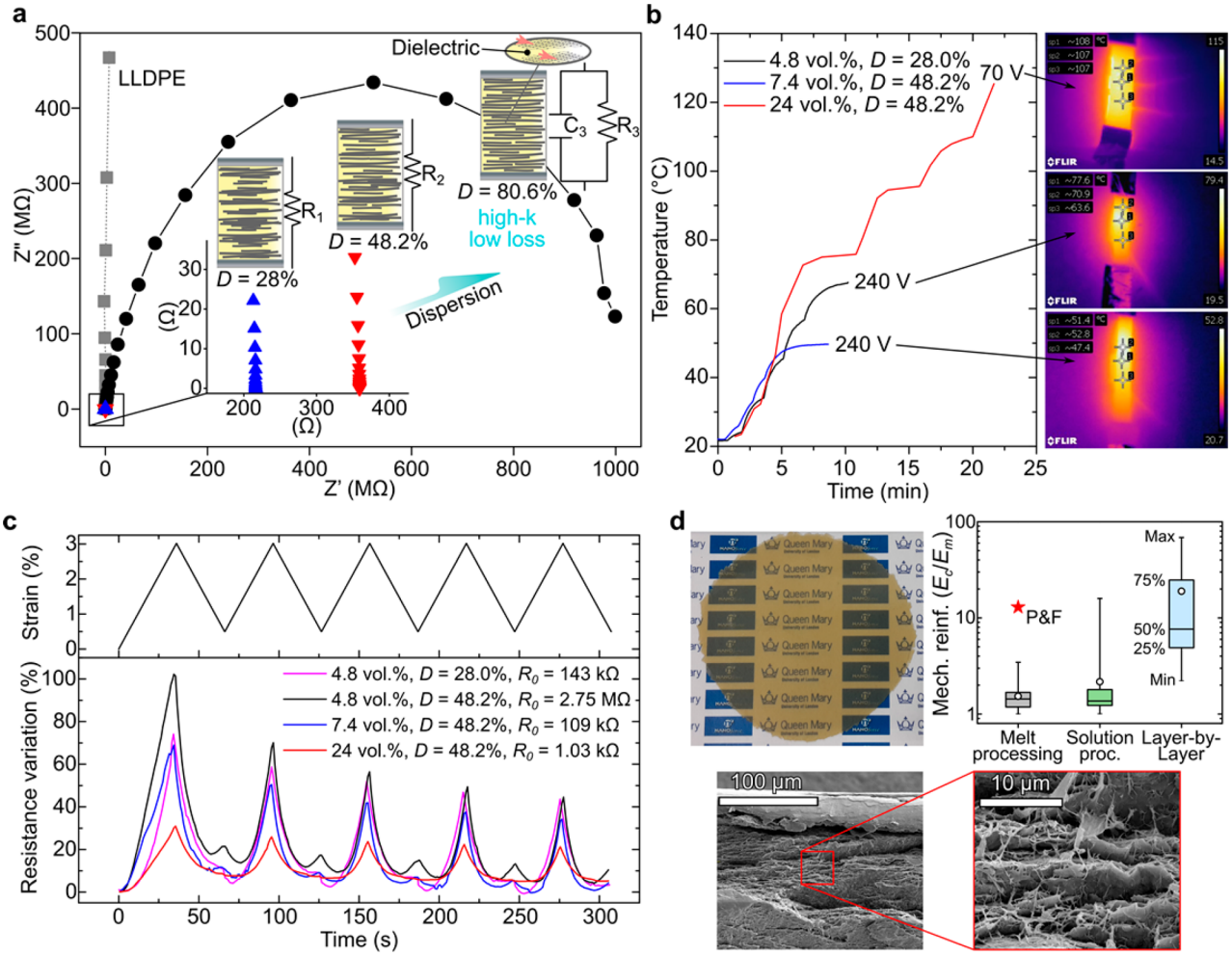

Figure 4. Examples of nanocomposites with optimized microstructures (nanofiller dispersion) for a variety of applications. (a) Imaginary (Z′′) *vs* real impedance (Z′) obtained from electrochemical impedance spectroscopy of LLDPE containing 4.8 vol % GNP for different dispersion levels. In accordance with value of σ_{th} expected from eq 5 the sample with D = 80.6% is the only one showing a capacitive effect, demonstrated by the Nyquist semicircle. (b) Self-heating originating from the Joule effect of LLDPE composites at different GNP loadings and dispersion levels. The sample with 4.8 vol % GNP shows a better self-heating effect than the sample containing 7.4 vol % GNP because its nanofiller dispersion level (D = 28) is closer to the critical value D_c= 25% predicted by eq 5. (c) Strain sensing of LLDPE composites with different GNP loadings and dispersion levels. High values of D give high resistance variations (gauge factor of ∼30) because the nanocomposite conductivity approaches the theoretical value σ_{th} more quickly with the strain (see sample containing 4.8 vol % GNP with D = 48.2%). Dispersions closer to D_c provide better electrical signals. The resistance variation becomes less evident for increasing amounts of GNP because the difference between σ_M and σ_{th} is smaller (for details, see section S.12.2 in the Supporting Information). (d) Optical picture (top left) of LLDPE containing 70 wt % MMT (∼10 cm wide and ∼400 μm thick), SEM cross-sections (bottom), and comparison (top right) of mechanical reinforcement with literature values for MMT nanocomposites grouped by the processing method. We achieved the highest mechanical reinforcement ever reported for melt processing. The QMUL logo is used with permission.

low electrical conductivity makes these nanocomposites promising for anisotropic thermal interface management of modern electronic, optoelectronic and photonic devices.[69]

High dispersion levels can be useful for energy-storage devices[25,26] (Figure 4a), provided that the electrical conductivity (σ_{th}) is small enough to allow huge polarization effects inside the layered microstructure without dielectric loss. A much-lower nanofiller dispersion (corresponding to the critical level D_c) is sufficient if high electrical conductivity is required, for example, in Joule-heating materials (Figure 4b) for de-icing[70] or safety self-limiting power devices.[23,24] An intermediate level of electrical conductivity, close to that corresponding to the percolation threshold, is normally required for resistive sensors (Figure 4c, for instance, shows the strain sensitivity of the nanocomposite) that could find applications in smart textile and structural health-monitoring applications.[29,30]

If a combination of properties is simultaneously desired, a compromise in nanofiller dispersion needs to be found. We found a good balance between mechanical and electrical properties when our GNP is ∼50% dispersed. At high nanofiller loadings, the theoretical conductivity at high dispersion states (σ_{th}) should not be very different from that at the critical dispersion level (σ_M). Therefore, one should find good electrical properties even if the nanofiller dispersion is greater than D_c. This is the case for our nanocomposites prepared with more than 20 vol % GNP, which appear to be simultaneously promising for self-heating devices triggered by low voltages (Figure 4b), health monitoring (Figure 4c), and mechanical applications.

DOI: 10.1021/acsnano.8b02877
ACS Nano 2018, 12, 9040−9050

To prove the general applicability of our technique to different filler−matrix combinations, a number of different nanocomposites were prepared by dispersing using P & F four types of nanoparticles of different shapes and sizes (GNP with low specific surface area, GNP with high specific surface area, montmorillonite MMT, and magnetite nanoparticles) into five different polymeric matrices. Independent from the specific filler−matrix system selected, nanofillers could always be efficiently dispersed into a given polymer matrix after a sufficient number of P & F cycles (section S.11.6 of the Supporting Information). The performance of the resulting material is extremely promising. Let us take a LLDPE containing MMT nanocomposite for example. Because we found a distribution rate of $\sim 7 \times 10^{-2}$ for MMT in LLDPE (much higher than $\sim 3 \times 10^{-3}$ for GNP), we expected to reach a dispersion of ∼99% after only ∼50 P & F cycles. Therefore, we prepared a sample containing an ultrahigh MMT loading of ∼74 wt %, and it appeared to be transparent indeed (Figure 4d) because of the good MMT dispersion and alignment. The nanocomposite had a Young's modulus of ∼1.8 GPa, approximately 13 times higher than that of the pure polymer. This is a surprisingly high value for a nanocomposite based on a commodity or engineering plastic prepared by a top-down technique (Figure 4d and section S.12.4 of the Supporting Information).

CONCLUSIONS

The lack of control over nanofiller dispersion, exacerbated at high nanofiller loadings, has often prevented nanocomposites from fulfilling multifunctional requirements. In this study, we have demonstrated a top-down scalable polymer processing method, the P & F method, that can enable the dispersion of ultrahigh concentrations of nanofiller (at least up to 74 vol %) by selecting a sufficient number of P & F cycles. With this method, we have been able to achieve mechanical reinforcements close to the maximum theoretical prediction levels, independent of nanofiller loading. Key aspects of the method are the controlled mixing, the use of a strong flow with a dominant elongational component, and the processing at temperatures just above the melting temperature. As an example of the potential of the method to optimize microstructures to achieve multifunctional properties, we have produced nanocomposites by P & F simultaneously presenting enhanced mechanical reinforcement, strain sensing, self-heating, and energy-management properties.

METHODS

Linear low-density polyethylene (density of 0.921 g/cm^3 and melting point of 116 °C), Flexirene MS20A (Versalis S.p.A., Italy), and the GNP (an expanded graphite of bulk density of 0.04 g/cm^3 and BET specific surface area of 25 m^2/g) Timrex C-Therm 002 (Timcal Ltd., Switzerland), were used as polymer matrix and nanofiller, respectively.

The P & F technique used to prepare the nanocomposites can be divided in three steps. First, two LLDPE films (∼100 μm thick) were prepared by hot-pressing polymer pellets inside a hot press (Collin P 300 E). Subsequently, GNP powder was deposited with a spatula in the middle of the surface of one LLDPE film so that the other film could be placed on top preventing the powder from spilling out. This "sandwich" was then hot-pressed inside of an aluminum frame (∼300 μm thick) at 40 bar and 120 °C for 30 s to join the two materials. In the final processing step, LLDPE and GNP were gradually dispersed by repetitive folding and hot-pressing these films. In particular, at each P & F cycle, the sample was manually folded twice in a symmetric manner and pressed at 40 bar and 120 °C for 30 s inside the aluminum frame to maintain the resulting thickness at ∼300 μm after the pressing. The weight concentration of GNP inside each sample was calculated by measuring the weight of the initial LLDPE films before and after adding GNP (after the second step).

To study the properties of the nanocomposites as a function of P & F cycles (corresponding to GNP dispersion and distribution throughout the matrix), samples of LLDPE containing 10.7 wt % (4.8 vol %) of GNP were prepared at different P & F cycles. To study the effect of possible degradation of the polymer matrix with the P & F cycles, samples of neat LLDPE at 1, 50, 100, and 150 P & F cycles were also prepared.

A reference sample of LLDPE containing 10.7 wt % of GNP was prepared by traditional melt-blending followed by a compression molding technique. Here, LLDPE pellets and GNP were used without drying. The composite was prepared by melt-blending at 120 °C under nitrogen atmosphere using a DSM X'plore 15 cm^3 micro compounder. Compounding was performed for 9 min at a screw speed of 180 rpm. The resulting compound was hot-pressed at 40 bar and 120 °C for 30 s inside an aluminum frame ∼300 μm thick.

Finally, samples of 0.5, 5, 10.7, 16, 43.6, and 56 wt % (corresponding to 0.21, 2.1, 4.8, 7.4, 24, and 35 vol %) of GNP were prepared at 200 P & F cycles to validate the effectiveness of this technique in dispersing different concentrations of nanofiller. It was chosen to prepare all samples at 200 P & F cycles because we found that this number of cycles gave optimal mechanical properties, which were even higher than those of the reference sample prepared by melt-blending, whereas electrical conductivity values were among the highest reported in literature.

The methods used to characterize the nanofiller, matrix, and nanocomposites are described in the Supporting Information. Methods used to test the self-heating effect, strain-sensing, and impedance and energy storage are also reported in the Supporting Information.

ASSOCIATED CONTENT

Supporting Information

The Supporting Information is available free of charge on the ACS Publications website at DOI: 10.1021/acsnano.8b02877.

Additional details on characterization techniques, XRD observations, nanofiller characterization, influence of P & F cycles, filler agglomerates inside nanocomposites, tensile failure, nanocomposites of LLDPE containing 4.8 vol % GNP prepared by melt blending, influence of GNP loading, rheology study, model derivation, potential applications, and an overview of classical composite theories (PDF)

AUTHOR INFORMATION

Corresponding Author

*E-mail: e.bilotti@qmul.ac.uk.

ORCID

Han Zhang: 0000-0002-0479-224X

Yan Li: 0000-0003-2503-1287

Samuele Colonna: 0000-0002-6409-227X

Nicola M. Pugno: 0000-0003-2136-2396

Emiliano Bilotti: 0000-0003-3952-1148

Author Contributions

E. Bilotti designed the experiments. G. Santagiuliana, L. Rubini, and Y. Li developed the P & F technique. G. Santagiuliana and L. Rubini prepared the P & F samples. O. T. Picot prepared the melt-blended reference sample. G. Santagiuliana and H. Zhang tested the strain-sensing behavior of samples. H. Porwal performed the self-heating tests and analyzed the related data. M. Crespo performed the EIS tests and analyzed the related data. S. Colonna and A. Fina

DOI: 10.1021/acsnano.8b02877
ACS Nano 2018, 12, 9040−9050

performed thermal conductivity tests. A. B. Spoelstra, G. Mirabello, and J. P. Patterson performed the transmission electron microscopy. G. Santagiuliana, O. T. Picot, and L. Rubini carried out all other samples characterizations. G. Santagiuliana, O. T. Picot, N. M. Pugno, T. Peijs, E. Barbieri, L. Botto, and E. Bilotti interpreted and discussed the results. G. Santagiuliana analyzed the data, derived the dispersion model and wrote the paper under the supervision of N. M. Pugno, T. Peijs, and E. Bilotti. L. Botto derived the micromechanical model of the P & F technique.

Notes

The authors declare no competing financial interest.

ACKNOWLEDGMENTS

This project has received funding from Innovate UK (KTP no. KTP009619) and the European Union's Seventh Framework Programme for research, technological development, and demonstration under grant agreement no. 604143. This project has also received funding from the EPSRC Grant Graphene 3D Networks (EP/K01658X/1). N. M. Pugno is supported by the European Commission under the Graphene Flagship Core 2 grant no. 785219 (WP14 "Composites") and FET Proactive "Neurofibers" grant no. 732344 as well as by the Italian Ministry of Education, University and Research (MIUR) under the "Departments of Excellence" grant no. L.232/2016. Activities by A. Fina and S. Colonna in this work were financially supported by the European Research Council (ERC) under the European Union's Horizon 2020 research and innovation programme under grant agreement no. 639495-INTHERM-ERC-2014-STG. E. Barbieri is supported by JSPS KAKENHI grant no. JP18K18065. The authors acknowledge S. Vidotto for helping with the preliminary characterization of the nanofiller, P. Rajamani for helping with the preparation of some samples, and R. Wilson for collecting the XRD patterns. LMK Thermosafe Ltd. is gratefully acknowledged as well as Nanoforce Technology Ltd. for use of facilities.

REFERENCES

(1) McEvoy, M. A.; Correll, N. Materials That Couple Sensing, Actuation, Computation, and Communication. *Science* **2015**, *347*, 1261689.

(2) Geim, A. K.; Novoselov, K. S. The Rise of Graphene. *Nat. Mater.* **2007**, *6*, 183−191.

(3) Lee, C.; Wei, X.; Kysar, J. W.; Hone, J. Measurement of the Elastic Properties and Intrinsic Strength of Monolayer Graphene. *Science* **2008**, *321*, 385−388.

(4) Bunch, J. S.; Verbridge, S. S.; Alden, J. S.; van der Zande, A. M.; Parpia, J. M.; Craighead, H. G.; McEuen, P. L. Impermeable Atomic Membranes from Graphene Sheets. *Nano Lett.* **2008**, *8*, 2458−2462.

(5) Novoselov, K. S.; Geim, A. K.; Morozov, S. V.; Jiang, D.; Zhang, Y.; Dubonos, S. V.; Grigorieva, I. V.; Firsov, A. A. Electric Field Effect in Atomically Thin Carbon Films. *Science* **2004**, *306*, 666−669.

(6) Balandin, A. A.; Ghosh, S.; Bao, W.; Calizo, I.; Teweldebrhan, D.; Miao, F.; Lau, C. N. Superior Thermal Conductivity of Single-Layer Graphene. *Nano Lett.* **2008**, *8*, 902−907.

(7) Nair, R. R.; Blake, P.; Grigorenko, A. N.; Novoselov, K. S.; Booth, T. J.; Stauber, T.; Peres, N. M. R.; Geim, A. K. Fine Structure Constant Defines Visual Transparency of Graphene. *Science* **2008**, *320*, 1308−1308.

(8) Young, R. J.; Kinloch, I. A.; Gong, L.; Novoselov, K. S. The Mechanics of Graphene Nanocomposites: A Review. *Compos. Sci. Technol.* **2012**, *72*, 1459−1476.

(9) Vlassiouk, I.; Polizos, G.; Cooper, R.; Ivanov, I.; Keum, J. K.; Paulauskas, F.; Datskos, P.; Smirnov, S. Strong and Electrically Conductive Graphene-Based Composite Fibers and Laminates. *ACS Appl. Mater. Interfaces* **2015**, *7*, 10702−10709.

(10) Liu, P.; Jin, Z.; Katsukis, G.; Drahushuk, L. W.; Shimizu, S.; Shih, C.-J.; Wetzel, E. D.; Taggart-Scarff, J. K.; Qing, B.; Van Vliet, K. J.; et al. Layered and Scrolled Nanocomposites with Aligned Semi-Infinite Graphene Inclusions at the Platelet Limit. *Science* **2016**, *353*, 364−367.

(11) May, P.; Khan, U.; O'Neill, A.; Coleman, J. N. Approaching the Theoretical Limit for Reinforcing Polymers with Graphene. *J. Mater. Chem.* **2012**, *22*, 1278−1282.

(12) Khan, U.; May, P.; O'Neill, A.; Bell, A. P.; Boussac, E.; Martin, A.; Semple, J.; Coleman, J. N. Polymer Reinforcement Using Liquid-Exfoliated Boron Nitride Nanosheets. *Nanoscale* **2013**, *5*, 581−587.

(13) Vaia, R. A.; Maguire, J. F. Polymer Nanocomposites with Prescribed Morphology: Going beyond Nanoparticle-Filled Polymers. *Chem. Mater.* **2007**, *19*, 2736−2751.

(14) Schaefer, D. W.; Justice, R. S. How Nano Are Nanocomposites? *Macromolecules* **2007**, *40*, 8501−8517.

(15) Sun, J.; Bhushan, B. Hierarchical Structure and Mechanical Properties of Nacre: A Review. *RSC Adv.* **2012**, *2*, 7617.

(16) Zhang, J.; Feng, W.; Zhang, H.; Wang, Z.; Calcaterra, H. A.; Yeom, B.; Hu, P. A.; Kotov, N. A. Multiscale Deformations Lead to High Toughness and Circularly Polarized Emission in Helical Nacre-like Fibres. *Nat. Commun.* **2016**, *7*, 10701.

(17) Kim, Y.; Yeom, B.; Arteaga, O.; Jo Yoo, S.; Lee, S.-G.; Kim, J.-G.; Kotov, N. A. Reconfigurable Chiroptical Nanocomposites with Chirality Transfer from the Macro- to the Nanoscale. *Nat. Mater.* **2016**, *15*, 461−468.

(18) Morgan, A. B. Flame Retarded Polymer Layered Silicate Nanocomposites: A Review of Commercial and Open Literature Systems. *Polym. Adv. Technol.* **2006**, *17*, 206−217.

(19) Kashiwagi, T.; Du, F.; Douglas, J. F.; Winey, K. I.; Harris, R. H.; Shields, J. R. Nanoparticle Networks Reduce the Flammability of Polymer Nanocomposites. *Nat. Mater.* **2005**, *4*, 928−933.

(20) Bourbigot, S.; Duquesne, S. Fire Retardant Polymers : Recent Developments and Opportunities. *J. Mater. Chem.* **2007**, *17*, 2283−2300.

(21) Holder, K. M.; Smith, R. J.; Grunlan, J. C. A Review of Flame Retardant Nanocoatings Prepared Using Layer-by-Layer Assembly of Polyelectrolytes. *J. Mater. Sci.* **2017**, *52*, 12923−12959.

(22) Costes, L.; Laoutid, F.; Brohez, S.; Dubois, P. Bio-Based Flame Retardants: When Nature Meets Fire Protection. *Mater. Sci. Eng., R* **2017**, *117*, 1−25.

(23) Rybak, A.; Boiteux, G.; Melis, F.; Seytre, G. Conductive Polymer Composites Based on Metallic Nanofiller as Smart Materials for Current Limiting Devices. *Compos. Sci. Technol.* **2010**, *70*, 410−416.

(24) Yi, X.-S.; Wu, G.; Pan, Y. Properties and Applications of Filled Conductive Polymer Composites. *Polym. Int.* **1997**, *44*, 117−124.

(25) Yuan, J.; Luna, A.; Neri, W.; Zakri, C.; Schilling, T.; Colin, A.; Poulin, P. Graphene Liquid Crystal Retarded Percolation for New High-k Materials. *Nat. Commun.* **2015**, *6*, 8700.

(26) Raccichini, R.; Varzi, A.; Passerini, S.; Scrosati, B. The Role of Graphene for Electrochemical Energy Storage. *Nat. Mater.* **2015**, *14*, 271−279.

(27) Blackburn, J. L.; Ferguson, A. J.; Cho, C.; Grunlan, J. C. Carbon-Nanotube-Based Thermoelectric Materials and Devices. *Adv. Mater.* **2018**, *30*, 1704386.

(28) Jones, W. E.; Chiguma, J.; Johnson, E.; Pachamuthu, A.; Santos, D. Electrically and Thermally Conducting Nanocomposites for Electronic Applications. *Materials* **2010**, *3*, 1478−1496.

(29) Thostenson, E. T.; Chou, T.-W. Real-Time *in Situ* Sensing of Damage Evolution in Advanced Fiber Composites Using Carbon Nanotube Networks. *Nanotechnology* **2008**, *19*, 215713.

(30) Luo, S.; Liu, T. Graphite Nanoplatelet Enabled Embeddable Fiber Sensor for *in Situ* Curing Monitoring and Structural Health Monitoring of Polymeric Composites. *ACS Appl. Mater. Interfaces* **2014**, *6*, 9314−9320.

DOI: 10.1021/acsnano.8b02877
ACS Nano 2018, 12, 9040−9050

(31) Li, X.; Yang, T.; Yang, Y.; Zhu, J.; Li, L.; Alam, F. E.; Li, X.; Wang, K.; Cheng, H.; Lin, C.-T.; Fang, Y.; Zhu, H. Large-Area Ultrathin Graphene Films by Single-Step Marangoni Self-Assembly for Highly Sensitive Strain Sensing Application. *Adv. Funct. Mater.* **2016**, *26*, 1322−1329.
(32) Picot, O. T.; Rocha, V. G.; Ferraro, C.; Ni, N.; D'Elia, E.; Meille, S.; Chevalier, J.; Saunders, T.; Peijs, T.; Reece, M. J.; Saiz, E. Using Graphene Networks to Build Bioinspired Self-Monitoring Ceramics. *Nat. Commun.* **2017**, *8*, 14425.
(33) Kashiwagi, T.; Fagan, J.; Douglas, J. F.; Yamamoto, K.; Heckert, A. N.; Leigh, S. D.; Obrzut, J.; Du, F.; Lin-Gibson, S.; Mu, M.; Winey, K. I.; Haggenmueller, R. Relationship between Dispersion Metric and Properties of PMMA/SWNT Nanocomposites. *Polymer* **2007**, *48*, 4855−4866.
(34) Mackay, M. E.; Tuteja, A.; Duxbury, P. M.; Hawker, C. J.; Van Horn, B.; Guan, Z.; Chen, G.; Krishnan, R. S. General Strategies for Nanoparticle Dispersion. *Science* **2006**, *311*, 1740−1743.
(35) Hooper, J. B.; Schweizer, K. S. Contact Aggregation, Bridging, and Steric Stabilization in Dense Polymer−Particle Mixtures. *Macromolecules* **2005**, *38*, 8858−8869.
(36) Hooper, J. B.; Schweizer, K. S. Theory of Phase Separation in Polymer Nanocomposites. *Macromolecules* **2006**, *39*, 5133−5142.
(37) Hall, L. M.; Jayaraman, A.; Schweizer, K. S. Molecular Theories of Polymer Nanocomposites. *Curr. Opin. Solid State Mater. Sci.* **2010**, *14*, 38−48.
(38) Keledi, G.; Hári, J.; Pukánszky, B. Polymer Nanocomposites: Structure, Interaction, and Functionality. *Nanoscale* **2012**, *4*, 1919.
(39) Šupová, M.; Martynková, G. S.; Barabaszová, K. Effect of Nanofillers Dispersion in Polymer Matrices: A Review. *Sci. Adv. Mater.* **2011**, *3*, 1−25.
(40) Mamedov, A. A.; Kotov, N. A.; Prato, M.; Guldi, D. M.; Wicksted, J. P.; Hirsch, A. Molecular Design of Strong Single-Wall Carbon Nanotube/Polyelectrolyte Multilayer Composites. *Nat. Mater.* **2002**, *1*, 190−194.
(41) Sui, L.; Huang, L.; Podsiadlo, P.; Kotov, N. A.; Kieffer, J. Brillouin Light Scattering Investigation of the Mechanical Properties of Layer-by-Layer Assembled Cellulose Nanocrystal Films. *Macromolecules* **2010**, *43*, 9541−9548.
(42) Sellam, C.; Zhai, Z.; Zahabi, H.; Picot, O. T.; Deng, H.; Fu, Q.; Bilotti, E.; Peijs, T. High Mechanical Reinforcing Efficiency of Layered Poly(Vinyl Alcohol) − Graphene Oxide Nanocomposites. *Nanocomposites* **2015**, *1*, 89−95.
(43) Luan, C. Baker's Transformation and Its Irreversibility. *Phys. Lett. A* **1991**, *152*, 6−10.
(44) Li, X.; McKenna, G. B.; Miquelard-Garnier, G.; Guinault, A.; Sollogoub, C.; Regnier, G.; Rozanski, A. Forced Assembly by Multilayer Coextrusion to Create Oriented Graphene Reinforced Polymer Nanocomposites. *Polymer* **2014**, *55*, 248−257.
(45) Affdl, J. C. H.; Kardos, J. L. The Halpin-Tsai Equations: A Review. *Polym. Eng. Sci.* **1976**, *16*, 344−352.
(46) Halpin, J. C.; Thomas, R. L. Ribbon Reinforcement of Composites. *J. Compos. Mater.* **1968**, *2*, 488−497.
(47) Turcsányi, B.; Pukánszky, B.; Tüdõs, F. Composition Dependence of Tensile Yield Stress in Filled Polymers. *J. Mater. Sci. Lett.* **1988**, *7*, 160−162.
(48) Voigt, W. Ueber Die Beziehung Zwischen Den Beiden Elasticitätsconstanten Isotroper Körper. *Ann. Phys.* **1889**, *274*, 573−587.
(49) Reuss, A. Berechnung Der Fließgrenze von Mischkristallen Auf Grund Der Plastizitätsbedingung Für Einkristalle. *Z. Angew. Math. Mech.* **1929**, *9*, 49−58.
(50) Wu, T.-L.; Lo, T.-S.; Kuo, W.-S. Effect of Dispersion on Graphite Nanosheet Composites. *Polym. Compos.* **2009**, *31*, 292−298.
(51) Wang, Y.; Shan, J. W.; Weng, G. J. Percolation Threshold and Electrical Conductivity of Graphene-Based Nanocomposites with Filler Agglomeration and Interfacial Tunneling. *J. Appl. Phys.* **2015**, *118*, 065101.
(52) Kim, H.; Kobayashi, S.; AbdurRahim, M. A.; Zhang, M. J.; Khusainova, A.; Hillmyer, M. A.; Abdala, A. A.; Macosko, C. W. Graphene/Polyethylene Nanocomposites: Effect of Polyethylene Functionalization and Blending Methods. *Polymer* **2011**, *52*, 1837−1846.
(53) Noorunnisa Khanam, P.; AlMaadeed, M. A.; Ouederni, M.; Harkin-Jones, E.; Mayoral, B.; Hamilton, A.; Sun, D. Melt Processing and Properties of Linear Low Density Polyethylene-Graphene Nanoplatelet Composites. *Vacuum* **2016**, *130*, 63−71.
(54) Tkalya, E.; Ghislandi, M.; Otten, R.; Lotya, M.; Alekseev, A.; van der Schoot, P.; Coleman, J.; de With, G.; Koning, C. Experimental and Theoretical Study of the Influence of the State of Dispersion of Graphene on the Percolation Threshold of Conductive Graphene/Polystyrene Nanocomposites. *ACS Appl. Mater. Interfaces* **2014**, *6*, 15113−15121.
(55) Li, J.; Kim, J.-K. Percolation Threshold of Conducting Polymer Composites Containing 3D Randomly Distributed Graphite Nanoplatelets. *Compos. Sci. Technol.* **2007**, *67*, 2114−2120.
(56) Barwich, S.; Coleman, J. N.; Möbius, M. E. Yielding and Flow of Highly Concentrated, Few-Layer Graphene Suspensions. *Soft Matter* **2015**, *11*, 3159−3164.
(57) Kuila, T.; Bose, S.; Mishra, A. K.; Khanra, P.; Kim, N. H.; Lee, J. H. Effect of Functionalized Graphene on the Physical Properties of Linear Low Density Polyethylene Nanocomposites. *Polym. Test.* **2012**, *31*, 31−38.
(58) Carotenuto, G.; De Nicola, S.; Palomba, M.; Pullini, D.; Horsewell, A.; Hansen, T. W.; Nicolais, L. Mechanical Properties of Low-Density Polyethylene Filled by Graphite Nanoplatelets. *Nanotechnology* **2012**, *23*, 485705.
(59) Vasileiou, A. A.; Kontopoulou, M.; Docoslis, A. A Noncovalent Compatibilization Approach to Improve the Filler Dispersion and Properties of Polyethylene/Graphene Composites. *ACS Appl. Mater. Interfaces* **2014**, *6*, 1916−1925.
(60) Gong, J.; Niu, R.; Liu, J.; Chen, X.; Wen, X.; Mijowska, E.; Sun, Z.; Tang, T. Simultaneously Improving the Thermal Stability, Flame Retardancy and Mechanical Properties of Polyethylene by the Combination of Graphene with Carbon Black. *RSC Adv.* **2014**, *4*, 33776−33784.
(61) Mittal, V.; Chaudhry, A. U. Polymer - Graphene Nanocomposites: Effect of Polymer Matrix and Filler Amount on Properties: Polymer - Graphene Nanocomposites: Effect of Polymer Matrix and Filler Amount on Properties. *Macromol. Mater. Eng.* **2015**, *300*, 510−521.
(62) Bilotti, E.; Zhang, R.; Deng, H.; Quero, F.; Fischer, H. R.; Peijs, T. Sepiolite Needle-like Clay for PA6 Nanocomposites: An Alternative to Layered Silicates? *Compos. Sci. Technol.* **2009**, *69*, 2587−2595.
(63) Kim, S.; Seo, J.; Drzal, L. T. Improvement of Electric Conductivity of LLDPE Based Nanocomposite by Paraffin Coating on Exfoliated Graphite Nanoplatelets. *Composites, Part A* **2010**, *41*, 581−587.
(64) Kuila, T.; Bose, S.; Hong, C. E.; Uddin, M. E.; Khanra, P.; Kim, N. H.; Lee, J. H. Preparation of Functionalized Graphene/Linear Low Density Polyethylene Composites by a Solution Mixing Method. *Carbon* **2011**, *49*, 1033−1037.
(65) Zhang, P.; Cao, D.; Cui, S. Resistivity-Temperature Behavior and Morphology of Low Density Polyethylene/Graphite Powder/Graphene Composites. *Polym. Compos.* **2014**, *35*, 1453−1459.
(66) Iqbal, M. Z.; Abdala, A. A.; Mittal, V.; Seifert, S.; Herring, A. M.; Liberatore, M. W. Processable Conductive Graphene/Polyethylene Nanocomposites: Effects of Graphene Dispersion and Polyethylene Blending with Oxidized Polyethylene on Rheology and Microstructure. *Polymer* **2016**, *98*, 143−155.
(67) Arora, A.; Padua, G. w. Review: Nanocomposites in Food Packaging. *J. Food Sci.* **2010**, *75*, R43−R49.
(68) Priolo, M. A.; Holder, K. M.; Greenlee, S. M.; Grunlan, J. C. Transparency, Gas Barrier, and Moisture Resistance of Large-Aspect-Ratio Vermiculite Nanobrick Wall Thin Films. *ACS Appl. Mater. Interfaces* **2012**, *4*, 5529−5533.

DOI: 10.1021/acsnano.8b02877
ACS Nano 2018, 12, 9040−9050

(69) Shahil, K. M. F.; Balandin, A. A. Graphene–Multilayer Graphene Nanocomposites as Highly Efficient Thermal Interface Materials. *Nano Lett.* **2012**, *12*, 861–867.
(70) Enríquez, E.; Fernández, J. F.; De Frutos, J.; De la Rubia, M. A. Tailoring of the Electrical Properties of Carbon Black–Silica Coatings for de-Icing Applications. *Ceram. Int.* **2015**, *41*, 2735–2743.

DOI: 10.1021/acsnano.8b02877
ACS Nano 2018, 12, 9040–9050

SUPPORTING INFORMATION

Breaking the Nanoparticle Loading/Dispersion Dichotomy in Polymer Nanocomposites with the Art of Croissant-Making

*Giovanni Santagiuliana[a], Olivier T. Picot[a,b], Maria Crespo[a], Harshit Porwal[a,b], Han Zhang[a,b], Yan Li[a,c], Luca Rubini[d], Samuele Colonna[e], Alberto Fina[e], Ettore Barbieri[a,f], Anne B. Spoelstra[g], Giulia Mirabello[g], Joseph P. Patterson[g], Lorenzo Botto[a], Nicola M. Pugno[d,h,a], Ton Peijs[a,b], Emiliano Bilotti[a,b] **

[a] School of Engineering and Materials Science, Queen Mary University of London, Mile End Road, London E1 4NS, U.K.

[b] Nanoforce Technology Limited, Mile End Road, London E1 4NS, U.K.

[c] Gemmological Institute, China University of Geosciences, 388 Lumo Rd., Wuhan, China 430074.

[d] Laboratory of Bio-inspired & Graphene Nanomechanics, Department of Civil, Environmental and Mechanical Engineering, University of Trento, Via Mesiano 77, 38123 Trento, Italy.

[e] Dipartimento di Scienza Applicata e Tecnologia, Politecnico di Torino, 15121 Alessandria, Italy.

[f] Japan Agency for Marine-Earth Science and Technology, Department of Mathematical Science and Advanced Technology, Yokohama Institute for Earth Sciences, 3173-25, Showa-machi, Kanazawa-ku, Yokohama-city, Kanagawa, 236-0001, Japan.

[g] Laboratory of Materials and Interface Chemistry & Centre for Multiscale Electron Microscopy

Department of Chemical Engineering and Chemistry, Eindhoven University of Technology, Eindhoven,

The Netherlands.

[h] Ket-Lab, Edoardo Amaldi Foundation, Italian Space Agency, Via del Politecnico, 00133 Rome, Italy.

Corresponding Author

* E-mail address: e.bilotti@qmul.ac.uk

Contents

S.1 Characterization techniques 4

S.2 X-ray diffraction (XRD) observations 9

S.3 Nanofiller characterization 11

S.4 Influence of P&F cycles on the properties of neat LLDPE 14

S.5 Influence of P&F cycles on the properties of LLDPE and GNP inside nanocomposites 15

S.6 Nanocomposites of LLDPE + 0.21 vol.% GNP at different P&F cycles: nanofiller distribution and microstructures 18

S.7 Nanocomposites of LLDPE + 4.8 vol.% GNP at different P&F cycles 19

S.7.1 Filler agglomeration 19

S.7.2 Fracture morphology 22

S.8 Nanocomposite of LLDPE + 4.8 vol.% GNP prepared by melt-blending 24

S.9 Influence of GNP loading on the properties of GNP and LLDPE inside nanocomposites prepared at 200 P&F cycles 25

S.10 Rheology study 27

S.11 Model derivation 31

S.11.1 Estimation of the shear-rate during P&F 31

S.11.2 Modelling of nanofiller dispersion and nanocomposite properties as a function of nanofiller dispersion level 34

S.11.3 Dispersion-factor for a melt-blending process 38

S.11.4 Dispersion-factor for a solution-mixing/casting process 38
S.11.5 Model fitting of P&F data 41
S.11.6 Another approach to estimate the distribution rates 42
S.12 Potential applications 46
S.12.1 Joule-heating 46
S.12.2 Strain sensing 47
S.12.3 Energy management 48
S.12.4 MMT nanocomposites 51
S.13 Classical composite theories 54
S.13.1 Halpin-Tsai model 54
S.13.2 Pukanszky model 55
S.14 References 55

S.1 Characterization techniques

The **lateral size** of the GNP powder particles was characterized by scanning electron microscopy (SEM, FEI Inspect-F). One hundred particles were measured for statistical determination of the particles' length and width. The length was considered as the longest side, whereas the width was measured along the normal of the length.

The **thickness** of GNP powder particles was characterized by atomic force microscopy (AFM, NT-MDT Ntegra) in semi-contact mode. The thickness of a particle was calculated by averaging the height profile. Twenty particles were measured for statistical determination of particles' thickness.

X-ray diffraction (XRD) studies were carried out at room temperature on a Panalytical X'Pert Pro diffractometer in reflection mode between 5°-70° 2θ and 2.5°-35° Ω, moving the samples with a spinner revolution time of 4 s. The X-ray tube used a tension of 45 kV, and 40mA of current. The incident beam employed the k-alpha1 radiation (0.154 nm) of the cupper anode. A filter made of nickel selected the diffracted beam. The crystalline interlayer spacing of GNP was determined by using Bragg's law:

$$d = \frac{\lambda}{2\sin(\theta)}$$

Equation S1.

where λ is the incident wavelength, and ϑ is the Bragg's angle of the (002) reflection around 26.6° 2θ. The mean thickness of GNP, and the mean sizes of the LLDPE crystallites were calculated with the Debye-Scherrer's formula:[1,2]

$$T = \frac{0.9\,\lambda}{\beta\cos(\theta)}$$

Equation S2.

where β is the full-width at half-maximum (FWHM) in radians of graphite (002) peak, or LLDPE (110) and (200) peaks around 21.6° 2θ and 23.8° 2θ, obtained from a single Gaussian peak fit between 20°-35° 2θ

for GNP powder, and from a multiple Gaussian peaks fit between 10°-35° 2θ for pure LLDPE and nanocomposites samples.

The degree of LLDPE crystallinity (X_c) was calculated from the integrated intensities of the (110) and (200) peaks, and from the area of the amorphous halo on which the crystalline peaks are superimposed, as described by the Hermans-Weidinger method:[2,3]

$$X_c = \frac{I_c^{110} + I_c^{200}}{I_a + I_c^{110} + I_c^{200}} \cdot 100$$

Equation S3.

The **microstructures** of the nanocomposites were studied by analysing the cross-sections of cryogenically broken samples by scanning electron microscopy (SEM, FEI Inspect-F). The specimens were previously gold-sputtered to cover them with a conductive film 6-8 nm thick. For statistical determination of filler agglomerates contained in nanocomposites of LLDPE + 4.8 vol.% GNP as a function of P&F cycles, diameter (the longest side) and thickness (segment along the normal of diameter) of each filler agglomerate was measured from at least three different specimen for each P&F sample, in order to have at least 100 measured agglomerates per sample. The aspect-ratio of each agglomerate was calculated by dividing its diameter by its thickness. The histograms of agglomerates' diameter, thickness, and aspect-ratio were fitted with a log-normal function in order to find out the geometrical mean values as a function of P&F cycles.

Electrical conductivity measurements were performed in-plane and out-of-plane of the samples by a 2-points probe connected to a DC system power supply (Agilent 6614c, 0-100V/0-0.5A), and a picoammeter (Keithely 6485, 2nA–20mA). A low electric field from 0 to 1.5 V/mm was applied in both cases in order to avoid a non-linear current-voltage relationship,[4] and 20 voltage-current data points were measured and recorded after waiting 100 ms at each 0.075 V/mm interval. Five specimens per sample were tested both for in-plane and out-of-plane measurements. Length (*L*), width (*W*), and

thickness (*T*) of each specimen were measured and recorded before testing (in particular, specimen 15×8×0.3 mm^3 of nominal size were used for in-plane, and 10×10×0.3 mm^3 for out-of-plane measurements). The electrical conductivity of each specimen, σ, was calculated after a linear fit of the current-voltage data:

$$\sigma = \frac{BL}{WT}$$

Equation S4.

where *B* is the slope of the fitting equation ($y = A + Bx$, with *y* = current, and *x* = voltage).

Tensile tests were executed following the ASTM D 638-02a standard method with specimen type V, performing five specimens per sample in a universal testing machine (Instron 5566), equipped with a 1 kN load cell. The experimental data points were collected every 10 ms. Width and thickness of each specimen were measured before testing. LLDPE samples were tested at 1 mm/min until a strain of 10% was reached, then the tests continued at 30 mm/min until failure. Nanocomposites and a reference sample of pure LLDPE were tested at 1 mm/min until breakage. The stress-strain curves were reconstructed using the collected load-extension data points and the specimens' sizes. The elastic modulus of each specimen was determined from the slope of a linear fit of the stress-strain curve executed over a strain range of 0.25% after the Toe's region. The yield point was considered as the first zero-slope point on the stress-strain curve.

Thermal diffusivity measurements were carried out using an incident lase pulse on the sample and recording temperature signal versus time with an IR detector. The thermal conductivity of the samples were calculated by multiplying the recorded thermal diffusivity with the samples' density and heat capacity (the latter was estimated by rule of mixture using a heat capacity of 1.555 J g^{-1} K^{-1} for LLDPE, and one of 0.709 J g^{-1} K^{-1} for GNP).

Joule/Self heating experiments were performed by applying a voltage using an AC power source from 0 to 240 V in steps. Current was recorded using a Tenma 72-7765 digital multimeter. Change in temperature on the sample surface was recorded with time by applying thermocouples to at least 3 different points. Thermal images of the samples were taken using a FLIR E40 thermal camera. The samples were placed in between insulating glass fibre mats to avoid heat loss.

Strain-sensing tests were performed using samples with nominal size of 50×0.3×15 mm^3 in a universal testing machine (Instron 5566), equipped with a 1 kN load cell. The grips were 20 mm far from each other at the beginning of each test. The extremities of the samples were previously coated with silver paint in order to assure a good electrical contact with a 2-points probe setup connected to a DC system power supply (Agilent 6614c, 0-100V/0-0.5A), and a picoammeter (Keithely 6485, 2nA–20mA). Two types of strain-sensing tests were conducted: cyclic tests consisting of stretching the samples between 0.5 and 3% of nominal strain for five times at a speed of 1 mm/min, and recording the resistance every second; and tensile tests at a speed of 1 mm/min until failure, recording the resistance every second.

Electrochemical impedance spectroscopy (EIS) measurements were performed between 100 mHz and 1 MHz using a SP-300 (SN 0623) Bio-Logic impedance analyser controlled by the EC-lab software. An AC-potential perturbation of 100 mV was used for all experiments. Nanocomposite films of ~300 µm in thickness were cut with a 1 cm diameter hole puncher. Round samples were placed between two full metallic electrodes that were tightened together with a screw press (*aka.* supercapacitor energy storage module). The permittivity of composites was determined from the impedance data according to:[5] $\varepsilon' \approx Z''/(Z''^2 + Z''^2)$ and $\varepsilon'' \approx Z'/(Z''^2 + Z''^2)$. As the shape factor (thickness/area) of all samples is equivalent, permittivity magnitudes were compared excluding this value.

Differential scanning calorimetry (DSC) analysis were performed on a TA Instruments DSC25 following this procedure:

- 1st DSC cycle: ramp 10 °C/min to -20.000 °C; isothermal 5.0 min; ramp 10 °C/min to 160.000 °C; isothermal 5.0 min; ramp 10 °C/min to -20.000 °C; isothermal 5.0 min;

- 2nd DSC cycle: ramp 10 °C/min to 160.000 °C; ramp 10 °C/min to -20.000 °C.

S.2 X-ray diffraction (XRD) observations

Figure S1 shows the XRD patterns of GNP powder, neat linear low density polyethylene (LLDPE) at different pressing and folding (P&F) cycles, nanocomposites of LLDPE + 0.21 vol.% of graphite nanoplatelets (GNP) at different P&F cycles, nanocomposites of LLDPE + 4.8 vol.% of GNP at different P&F cycles, and a nanocomposite of LLDPE + 35 vol.% of GNP at 200 P&F cycles. All the details of these XRD patterns are presented in Table S1.

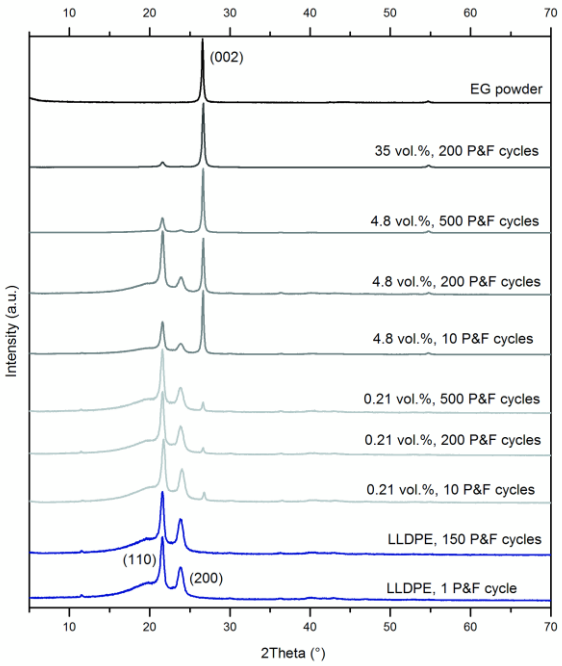

Figure S1. XRD patterns of GNP powder, neat LLDPE, and LLDPE nanocomposites containing specified GNP loadings.

Table S1. Values found or calculated from all the XRD patterns of Figure S1.

Sample	P&F cycles	GNP (002) peak (° 2θ)	$\overline{t}$ of GNP (nm)	LLDPE crystallite size from (110) peak (nm)	LLDPE crystallite size from (200) peak (nm)	LLDPE crystallinity, X_c (%)
GNP powder		26.57	27			
LLDPE	1			16.6	11.1	32.4 ± 0.6
	150			16.9	11.2	33.4 ± 0.4
LLDPE + 0.21 vol.% GNP	10	26.77	26	16.5	11.1	32.5 ± 0.4
	200	26.63	33	17.3	11.1	31.5 ± 0.4
	500	26.63	31	17.3	11.0	33.1 ± 0.5
LLDPE + 4.8 vol.% GNP	10	26.62	28	17.4	11.6	34.0 ± 0.6
	200	26.66	26	17.5	11.3	36.6 ± 0.6
	500	26.63	28	18.1	12.5	36.7 ± 1.3
LLDPE + 35 vol.% GNP	200	26.66	27	15.0	11.0	40 ± 4

S.3 Nanofiller characterization

Figure S2 shows the SEM and AFM observations of the as received GNP powder. The particles appeared to be irregularly shaped (see Figure S2a), probably resulting from the aggregation of smaller sub-particles, as suggested by the observation in Figure S2b.

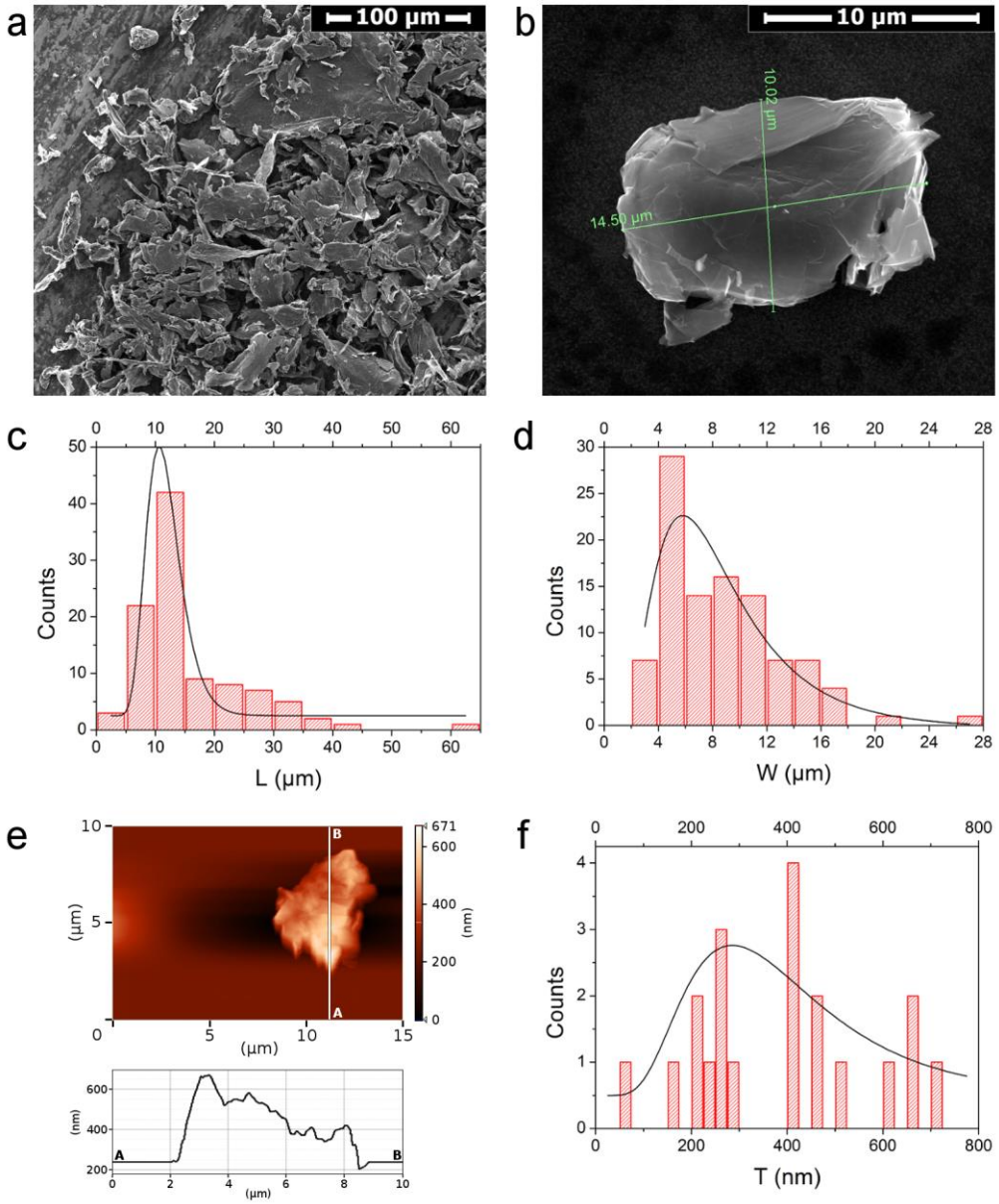

*Figure S2. SEM images of GNP powder (**a**-**b**); size distributions of the longest and shortest sides obtained from SEM measurements of 100 GNP powder particles (**c**-**d**); AFM image of an GNP powder particle with the thickness profile of the highlighted AB line (**e**); and thickness distribution obtained from AFM measurements of 20 GNP powder particles (**f**).*

Parts c and d of Figure S2 show the size distributions of the longest (L) and shortest (W) sides of 100 GNP powder particles. These distributions were fitted with a log-normal function,[6] obtaining the following geometric mean values (that is, the median of each distribution) and geometric standard deviations (GSD): $\overline{L}$ = 11.4 μm with GSD_L = 1.3, and $\overline{W}$ = 7.8 μm with GSD_W = 1.7. Note that the geometric coefficient of variation is 30% for L, and 72% for W, meaning that the distribution of the shortest particle side is more broadened. Since most of the measured particles (63%) have a W/L ratio greater than 0.5, the GNP powder particles can be approximated to disc-like particles with a mean diameter $\overline{D} = \sqrt{\overline{LW}}$ = 9.4 μm.

The thickness distribution of the GNP powder particles is shown in Figure S2f, and was fitted with a log-normal function, obtaining the following values: $\overline{T}$ = 364 nm, GSD_T = 1.6. The geometric coefficient of variation of T is high: 64%, mainly because of the low number of measurements (20), and the irregular thickness of each particle (see the thickness profile of the particle in Figure S2e), probably due to some folded sides, or different numbers of agglomerated sub-particles, as suggested before.

The density of these GNP powder particles cannot be measured, so the volume fractions occupied by these GNP powder particles inside the nanocomposites cannot be calculated. However, the density of pure graphite, d_G = 2.2 g/cm^3,[7] can be attributed approximatively. In this way, by using d_G and the above-mentioned values of $\overline{D}$ and $\overline{T}$, it is possible to calculate a specific surface area of $\frac{\pi\overline{D}^2/2+\pi\overline{D}\overline{T}}{d_G\pi\overline{D}^2\overline{T}/4} = 2.7$ m^2/g for GNP, which is much lower than the reported BET surface area (25 m^2/g). This confirms the initial hypothesis that the observed GNP powder particles are made of agglomerated sub-particles (for example graphite nanoplatelets, GNP).

The density and thickness of these sub-particles can be deduced from the XRD pattern of GNP powder (Figure S1).[8] The graphite (002) peak centred on 26.6° 2θ (see Table S1 for details of the XRD pattern)

corresponds to an interlayer spacing of 0.335 nm. This value is in good agreement with the *d*-spacing of bulk graphite,[9–11] thus the density is the same one as for pure graphite. From the (002) peak, a thickness $\overline{t}$ of ~27 nm can also be calculated, which can be confirmed by the BET specific surface area (assuming that the lateral area of each particle is negligible because the particle diameter is much larger than the particle thickness): $\overline{t} \approx 2/(d_G \cdot S_{BET})$ = 36 nm. This is a clear evidence of the presence of GNP, and the GNP volume fractions inside nanocomposites can be certainly converted from the weight fractions by using the density of pure graphite, d_G.

It is possible to calculate the maximum effective Young's modulus of the filler, E_{GNP}^{eff}, from the value of the crystallographic thickness of GNP, as suggested by Gong *et al.*:[12]

$$E_{GNP}^{eff} = \frac{E_{graphene}}{\frac{n_l}{2} - k_i\left(\frac{n_l}{2} - 1\right)}$$

Equation S5.

where $E_{graphene}$ ≈ 1000 GPa, n_l is the average number of graphene layers stacked inside the GNP (~100 for our GNP), and k_i is a stress transfer efficiency factor between the layers (≈ 0.7). For our filler, the effective Young's modulus according to Equation S5 yields ~65 GPa. This is a reasonable value if compared to the results of Krzesinska *et al.*, who studied the elastic modulus of expanded graphite powders with different porosities using ultrasound measurements, and found that the maximum elastic modulus of completely compressed expanded graphite (without any porosity) is about 30 GPa.[7]

S.4 Influence of P&F cycles on the properties of neat LLDPE

The P&F technique consists of pressing a thermoplastic polymer with a nanofiller at a temperature slightly above the polymer's melting point, thus the polymer should recover its initial properties after cooling down to ambient temperature. It is worth noting that the P&F was performed in air, and in order to assess any effect of thermal degradation on the alteration of polymer properties, samples of pure LLDPE were prepared at 1, 50, 100, and 150 P&F cycles. Tensile tests revealed that the properties (Young's modulus, yield stress, and ultimate tensile stress) of pure LLDPE at different numbers of P&F cycles were relatively unaffected by the P&F technique up to 150 P&F cycles (see Figure S3). Therefore, the sample prepared at the first P&F cycle was used as reference sample for comparison with nanocomposites' properties.

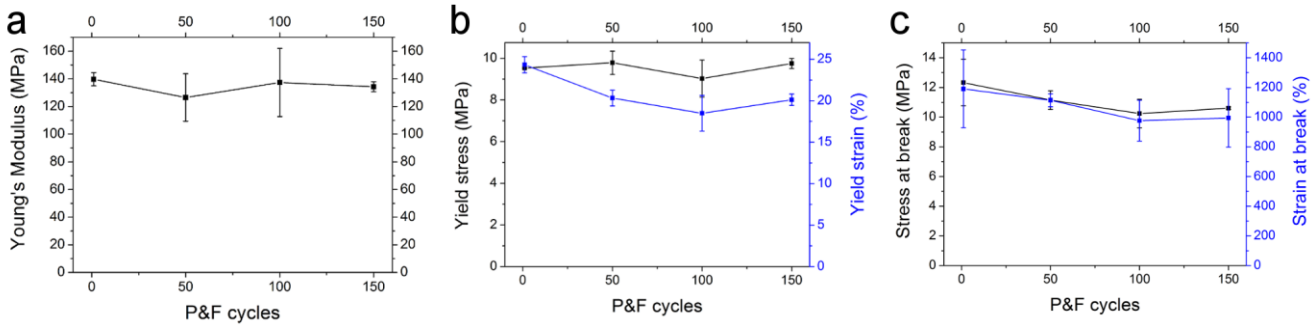

*Figure S3. Young's modulus (**a**), yield (**b**), and break point (**c**) of neat LLDPE samples prepared at different P&F cycles.*

The XRD pattern of pure LLDPE (Figure S1) shows two diffraction peaks around 21.6° 2θ and 23.8° 2θ due to the (110) and (200) reflections superimposed to an amorphous halo.[13,14] The crystallinity was ~33% for both samples prepared at one and 150 P&F cycles (Table S1). The crystallites size calculated from the (110) and (200) peaks were of 17 nm and 11 nm, for both samples. These findings suggest that the P&F technique up to 150 P&F cycles has little effect on the properties of neat LLDPE. Moreover,

Table S1 shows that a sample of LLDPE containing a small amount of GNP (0.21 vol.%) did not change its crystallinity up to 500 P&F cycles, confirming that the properties of LLDPE are not significantly influenced by the P&F technique.

S.5 Influence of P&F cycles on the properties of LLDPE and GNP inside nanocomposites

It was shown above how the P&F technique itself does not significantly influence the properties of neat LLDPE, however, the presence of GNP together with the effect of the pressing and folding cycles could change its crystallinity. This is important because LLDPE of higher crystallinity has an increased Young's modulus and yield stress, but lower tensile strength and elongation at break.[2]

Nanocomposites containing 4.8 vol.% of GNP showed that the LLDPE crystallite sizes and crystallinity increased slightly with the number of P&F cycles (Table S1). However, referring to the findings of Kundu *et al.*, a relative increase of ~8% in crystallinity found for the sample at 500 P&F is too low to significantly alter the mechanical properties of LLDPE.[2] Therefore, an eventual improvement of the nanocomposite's mechanical properties should be attributed mainly to an improved reinforcing efficiency of the nanofiller as a result of an improvement in nanofiller distribution and dispersion rather than an increase of polymer crystallinity.

We analysed these samples also by DSC (Figure S4), together with a highly loaded sample for comparison. We found that the nanofiller dispersion level slightly affect the crystallinity (see data in Table S4 for samples prepared after 50 and 200 P&F cycles). The amount of GNP has a similar effect (Table S4). However, these changes are negligible, so any improvement in the nanocomposite mechanical properties mast be caused by an increased nanofiller-matrix interface.

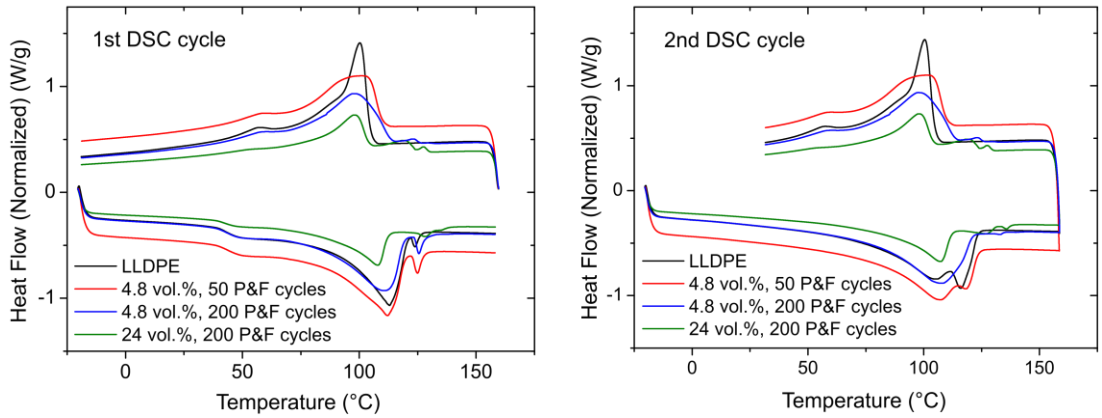

Figure S4. DSC analysis.

Table S2. Values found from the first DSC cycle of Figure S4.

SAMPLE	Heating			Cooling		
	Peak temp. (°C)	Enthalpy (J/g)	Onset temp (°C)	Peak temp. (°C)	Enthalpy (J/g)	Onset temp (°C)
4.8 vol%, 50 P&F cycles	112.19	70.319	89.88	102.57	63.516	109.83
4.8 vol.%, 200 P&F cycles	110.93	71.202	83.95	98.49	58.582	113.38
24 vol.%, 200 P&F cycles	110.93	71.202	83.95	98.49	58.882	113.38
LLDPE pristine	112.96	75.807	90.74	100.32	74.39	104.74

Regarding the GNP characteristics, the graphite diffraction peak did not change its position with the number of P&F cycles, meaning that the crystalline interlayer spacing and the density of GNP was unaffected by the P&F cycles. Likewise, since the (002) peak did not shift to lower 2θ values as it happens for graphite oxide,[11,15–18] no oxidation of GNP is expected to take place during the P&F process. Furthermore, the thickness of GNP remained the same with P&F cycles, meaning that there was no exfoliation of GNP during the process, thus any variation in the properties of the nanocomposites with

P&F cycles must be caused only by improved distribution and dispersion of the nanofiller, rather than an increase in GNP aspect-ratio.

All the above observations are confirmed by the samples of LLDPE containing 0.21 vol.% of GNP. No relevant changes in LLDPE crystallite sizes and crystallinity with the number of P&F cycles was present (Table S1), that is, the matrix properties are not influenced by the P&F technique. The graphite diffraction peak did not modify its position with the number of P&F cycles, meaning that the density of GNP was unaffected by the P&F cycles, and that GNP did not oxidize during the hot-pressing steps. Furthermore, the thickness of GNP remained the same with P&F cycles, viz. there was no exfoliation of GNP during the process.

S.6 Nanocomposites of LLDPE + 0.21 vol.% GNP at different P&F cycles: nanofiller distribution and microstructures

Figure S5a shows a macroscopic visualization of the effect of the P&F technique on the distribution of GNP throughout the specimen of a series of samples containing 0.21 vol.% of GNP. The colour of these samples became darker with P&F cycles because of better nanofiller dispersion and distribution. Figure S5b shows the microstructures of these nanocomposites at different P&F cycles. At low P&F cycles, the microstructures show large GNP agglomerates with a thickness nearly the same as the film sample, which decreased in thickness and width with P&F cycles. Eventually, at 500 P&F the particles were well distributed, dispersed and oriented parallel to the plane of the film samples.

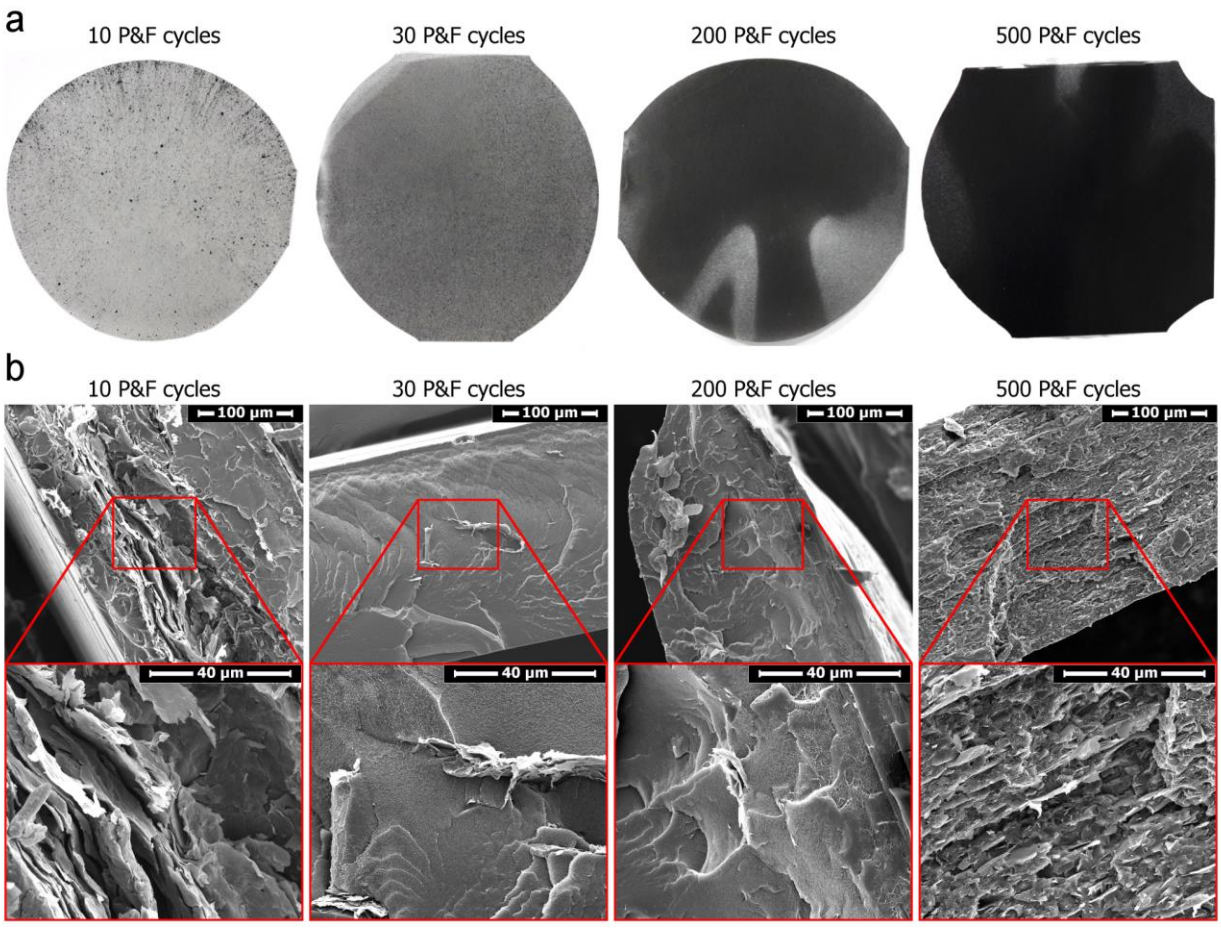

*Figure S5. Pictures (**a**) and SEM images (**b**) of the cross-sections of LLDPE + 0.21 vol.% GNP samples at different P&F cycles. The samples were about 8 cm in diameter, and 300 µm thick.*

S.7 Nanocomposites of LLDPE + 4.8 vol.% GNP at different P&F cycles

S.7.1 Filler agglomeration

The microstructure of nanocomposites of LLDPE + 4.8 vol.% GNP was systematically studied at different P&F cycles in order to find out the break-down of filler agglomerates during the P&F process. Figure S6a shows a macroscopic visualization of the effect of the P&F technique on the distribution of GNP throughout the specimen. The first P&F cycles break down initially the large agglomerates. Because of the high GNP concentration, the samples appeared homogeneous to the naked eye already after 20-30 P&F cycles, differently to the series of samples with lower GNP concentration (0.21 vol.%). Figure S6b shows how the microstructure of the same nanocomposites changes as a function of P&F cycles, whereas Figure S6c presents the geometrical mean values of aspect-ratio, diameter, and thickness of filler agglomerates obtained from the statistical distributions of the agglomerates measured from the samples' microstructures (see Figure S7). At 10 P&F cycles, there were large GNP agglomerates with thicknesses close to those of the disk film samples (ca. 300 μm). These agglomerates decreased in thickness and diameter very quickly with increasing P&F cycles up to 50 P&F cycles, with particles inside the agglomerates appearing to be mainly oriented parallel to the plane of the samples. Between 50 and 200 P&F cycles, it was difficult to find GNP agglomerates, and many dispersed particles appeared throughout the matrix volume. Eventually, the microstructure at 500 P&F cycles was clearly well-ordered with homogeneously distributed and well dispersed particles oriented parallel to the plane of the film samples.

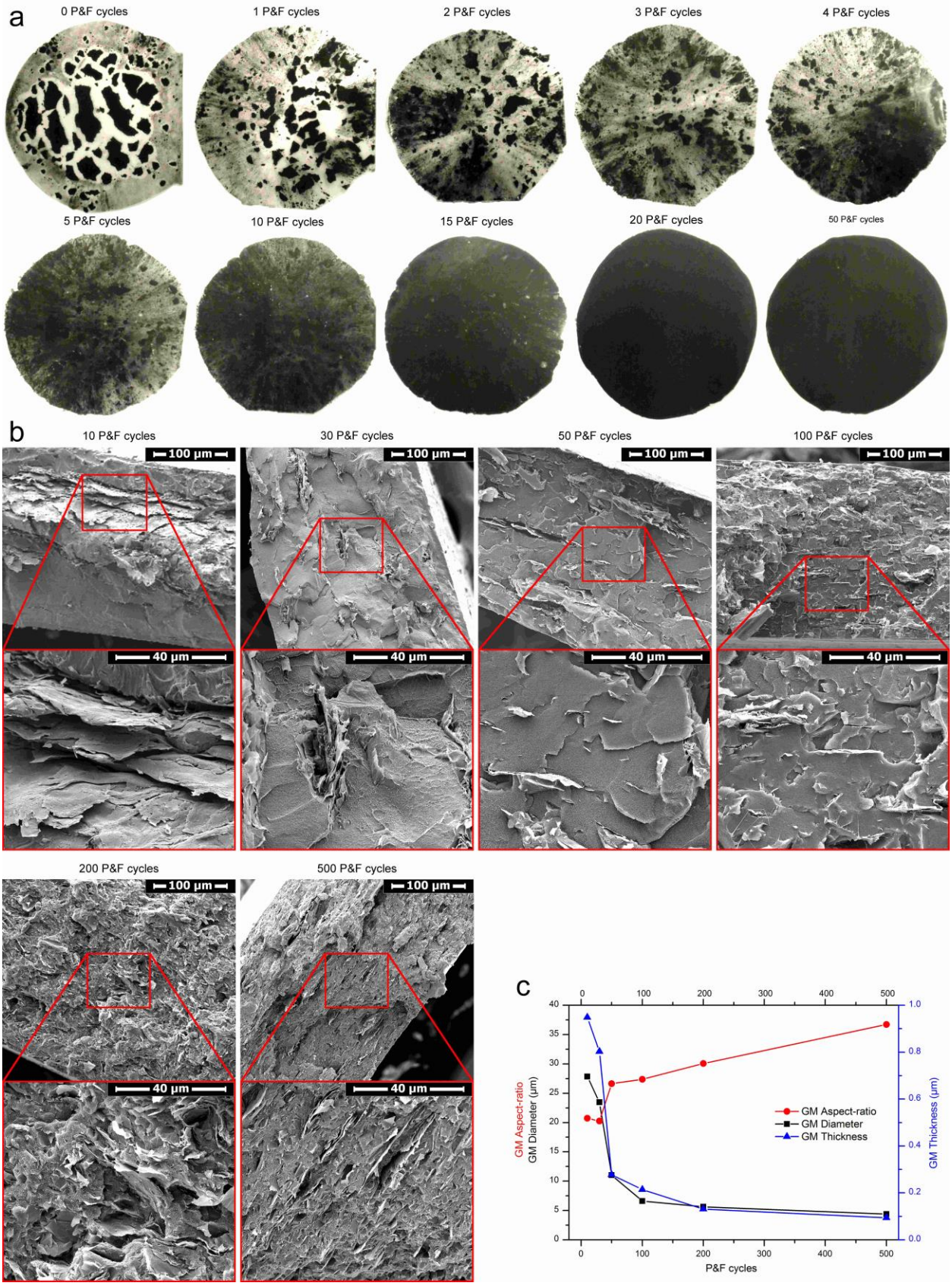
a
0 P&F cycles
1 P&F cycles
2 P&F cycles
3 P&F cycles
4 P&F cycles
5 P&F cycles
10 P&F cycles
15 P&F cycles
20 P&F cycles
50 P&F cycles
b
10 P&F cycles
30 P&F cycles
50 P&F cycles
100 P&F cycles
200 P&F cycles
500 P&F cycles
100 μm
40 μm
c
GM Aspect-ratio
GM Diameter
GM Thickness
GM Aspect-ratio (μm)
GM Diameter (μm)
GM Thickness (μm)
P&F cycles

*Figure S6. (**a**) Pictures of LLDPE + 4.8 vol.% GNP samples at different P&F cycles, (**b**) SEM images of the cross-sections of LLDPE + 4.8 vol.% GNP samples, and (**c**) geometrical mean values of filler agglomerate's aspect-ratio, diameter and thickness as a function of P&F cycles. Film samples were about 8 cm in diameter, and 300 µm thick.*

Figure S7 shows the statistical distributions of diameter, thickness, and aspect-ratio of the agglomerates at different P&F cycles. The geometrical means of these distributions are reported in Table S3 together with their geometrical standard deviations, and displayed in Figure S6c. The mean diameter and thickness decreased drastically at the first ~50 P&F cycles (see also Figure S6c), and they further reduced to the size of single GNPs after 500 P&F cycles, meaning that a good dispersion of nanoparticles was reached at this high number of P&F cycles without any significant agglomeration. In fact, the geometrical mean thickness of the filler at 500 P&F cycles (~90 nm) is fairly close to the thickness of GNP (~30 nm). Conversely, the aspect-ratio of the agglomerates does not change significantly with the P&F cycles as diameter and thickness do, and it only doubles its initial value after 500 P&F cycles.

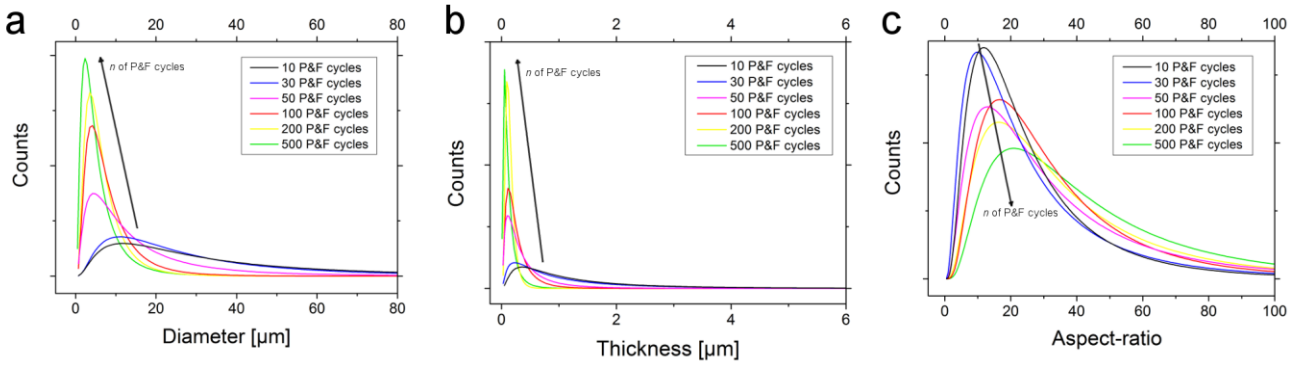

*Figure S7. Statistical distributions of (**a**) diameter, (**b**) thickness, and (**c**) aspect-ratio of filler agglomerates in nanocomposites of LLDPE + 4.8 vol.% GNP at different P&F cycles.*

Table S3. Geometrical means (GM) and geometrical standard deviations (GSD) related to the distributions of Figure S7.

P&F cycles	Diameter		Thickness		Aspect-ratio	
	GM (μm)	GSD	GM (μm)	GSD	GM	GSD
10	27.9	2.54	0.948	2.70	20.7	2.12
30	23.5	2.39	0.803	3.06	20.2	2.33
50	11.0	2.58	0.278	2.64	26.6	2.34
100	6.60	2.02	0.214	2.15	27.4	2.04
200	5.64	1.96	0.131	1.66	30.1	2.18
500	4.37	2.21	0.093	2.36	36.7	2.11

S.7.2 Fracture morphology

Figure S8 shows the fracture surfaces of LLDPE + 4.8 vol.% GNP samples prepared at different P&F cycles. At low number of P&F cycles, the fracture surfaces show GNP agglomerates with thicknesses almost as thick as the film samples (Figure S8a). Such large agglomerates were not visible in cryogenically broken specimen. This can be explained by the fact that failure was initiated by the widest agglomerates because of stress concentrations in the polymer matrix (the agglomerates cannot carry the applied load because they are not a continuum body). In fact, samples prepared below 50 P&F cycles typically showed some GNP dust coming from the fracture surface, indicating that the GNP powder was not fully embedded in the polymer. The consequence of this was that the tensile strength of these samples was lower than that of pure LLDPE. For example, the sample prepared at 10 P&F cycles contained some wide agglomerates up to ~1/4 of the fracture surface area, and its stress at break was 7 MPa (stress at break of pure LLDPE was 9.5 MPa). If the cross-section relative to LLDPE is used for the calculation of the stress at break, than the stress at break gives ~7 MPa / (1–1/4) = 9.3 MPa, which is the stress at break of pure LLDPE. Samples prepared above 150 P&F cycles did not present any GNP agglomerates in the fracture surfaces, and their stresses at break were higher than that of pure LLDPE.

Moreover, the fracture surface of these samples appeared smooth and regular with short LLDPE fibrils disposed in layers (Figure S8b). On the contrary, samples prepared at low P&F cycles presented irregularly shaped fracture surfaces, with wide and long strained LLDPE fibrils, which were similar to those observed in pure LLDPE samples.

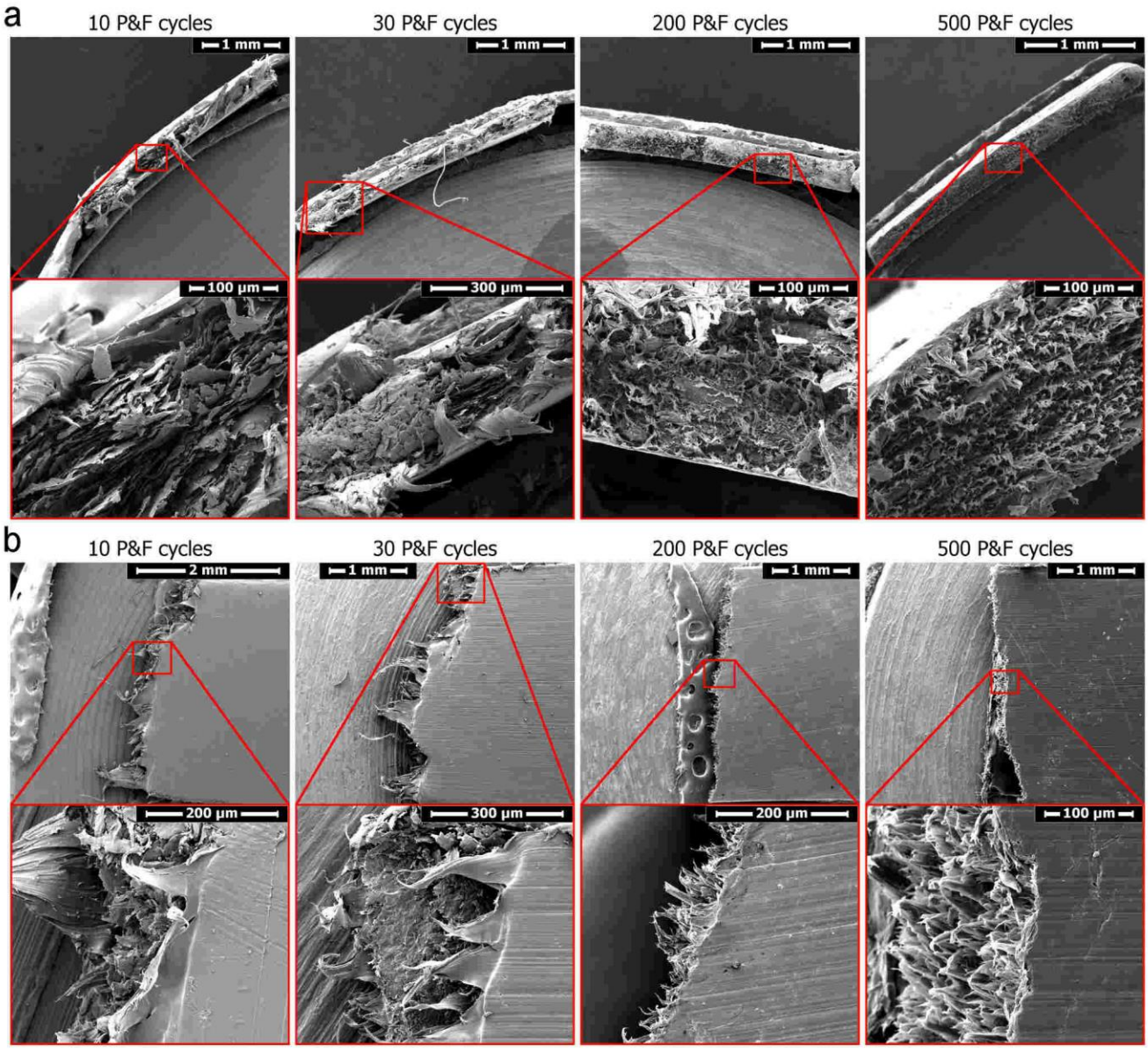

*Figure S8. Front view (**a**) and side view (**b**) of the tensile fracture surfaces of LLDPE + 4.8 vol.% GNP samples prepared at different P&F cycles.*

S.8 Nanocomposite of LLDPE + 4.8 vol.% GNP prepared by melt-blending

Figure S9 shows the microstructure of a LLDPE nanocomposite prepared by melt-blending containing 4.8 vol.% of GNP. Different from the microstructures of nanocomposites prepared by P&F, the particles appear more 3D randomly oriented, but no large agglomerates are present, as in samples prepared above 200 P&F cycles.

Tensile tests revealed a mechanical reinforcement (E_c/E_m) of 1.4 ± 0.3, which is equivalent to samples prepared by 100 P&F cycles, a yield stress of 9.9 ± 0.9 MPa and an ultimate tensile stress of 9.4 ± 1.1 MPa, similar to samples prepared at 150 P&F cycles. The tensile fracture surface (Figure S9) is straight as it happens for P&F samples above 100 P&F cycles, and the LLDPE fibrils after failure have a similar morphology of those observed in the P&F sample prepared at 200 P&F cycles.

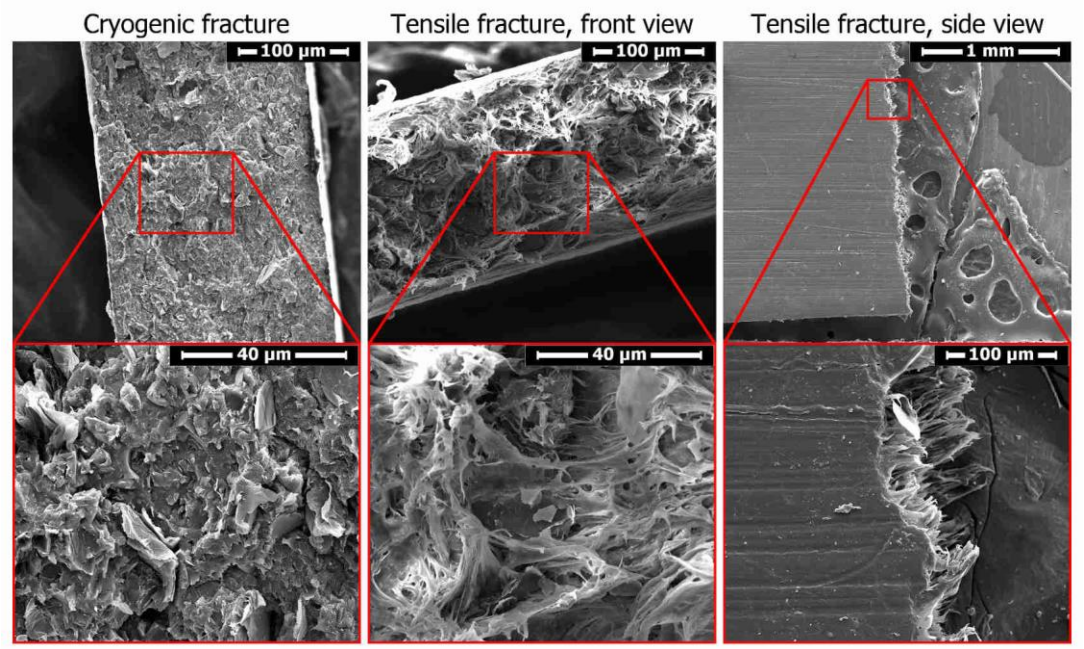

Figure S9. Cryogenic and tensile fracture surfaces of a LLDPE + 4.8 vol.% GNP sample prepared by melt-blending and compression moulding.

S.9 Influence of GNP loading on the properties of GNP and LLDPE inside nanocomposites prepared at 200 P&F cycles

As reported in Table S1, the LLDPE crystallite sizes remained almost the same for samples prepared at 200 P&F cycles containing three different amounts of GNP (0.21, 4.8, and 35 vol.%): there was only a small decrease from 17 nm to 15 nm for the crystallite size related to the (110) peak of the sample containing 35 vol.% of GNP. The LLDPE crystallinity increased with the amount of GNP. These findings are in contrast with what is reported in literature: the addition of nanofiller slightly increased the LLDPE crystallite sizes,[1] and decreased the degree of crystallinity,[1,13] because of a random interface between nanofiller and matrix, which "inhibited the ordered crystalline structure of the polymer chains".[1] Other studies indicated that the LLDPE crystallinity calculated from differential scanning calorimetry (DSC) measurements did not change with the amount of GNP,[19] or with the amount of graphene.[18] Therefore, the P&F technique might help the LLDPE polymer chains to arrange themselves in a crystalline structure among graphite nanoparticles. However, referring to the findings of Kundu *et al.*, a relative increase of ~22% in crystallinity compared with pure LLDPE was found for the sample containing 35 vol.% of GNP is too low to significantly alter the mechanical properties of LLDPE.[2]

Eventually, the position of the graphite (002) peak and the thickness of GNP remained the same as a function of the amount of GNP in the samples, meaning that there was no change in the intrinsic properties of GNP during the processing of these nanocomposites.

Representative stress-strain curves of nanocomposites prepared at 200 P&F cycles with different GNP loadings are presented in Figure S10. The strain at break abruptly decreases with the GNP amount, and the sample containing 35 vol.% GNP clearly does not show any yield before fracture.

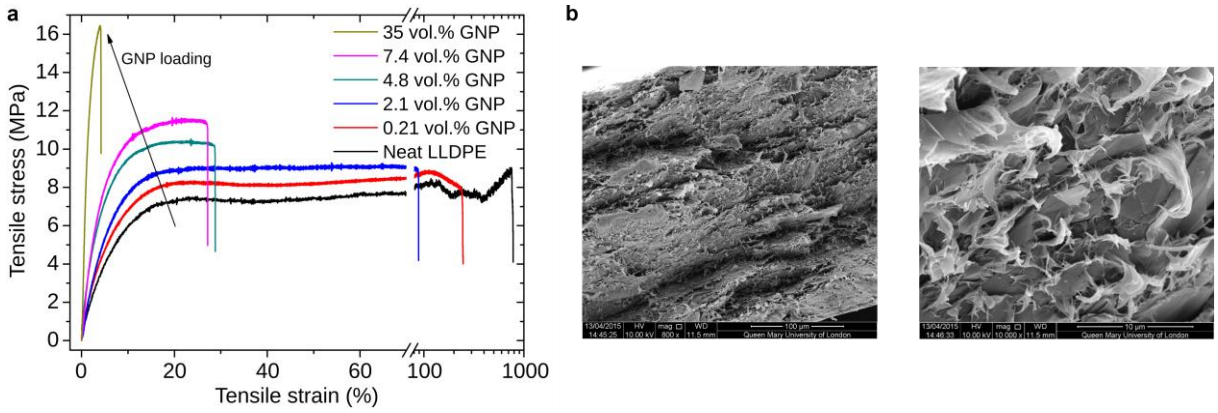

*Figure S10. (**a**) Representative stress-strain curves of GNP-LLDPE nanocomposites prepared with 200 P&F cycles and different GNP loadings. (**b**) SEM cross-sections of LLDPE + 35 vol.% GNP after 200 P&F cycles: the microstructure contains aligned and well dispersed GNP despite the high GNP concentration.*

S.10 Rheology study

Viscosity of P&F samples containing 4.8 vol.% GNP at different temperatures

The P&F technique was performed at a temperature (120 °C) really close to the melting point of the polymer (116 °C), differently from melt-blending techniques that use temperatures around 190 °C for LLDPE. This has a consequence on the viscosity of the samples, which results much higher than what it should be if the samples were processed at higher temperatures.

The graphs below show the viscosity of the P&F samples containing 4.8 vol.% GNP at 120 °C, 140 °C, and 180 °C. Note that the viscosity of neat LLDPE decreases from ~4.000 Pa.s at 120 °C to ~350 Pa.s at 180 °C.

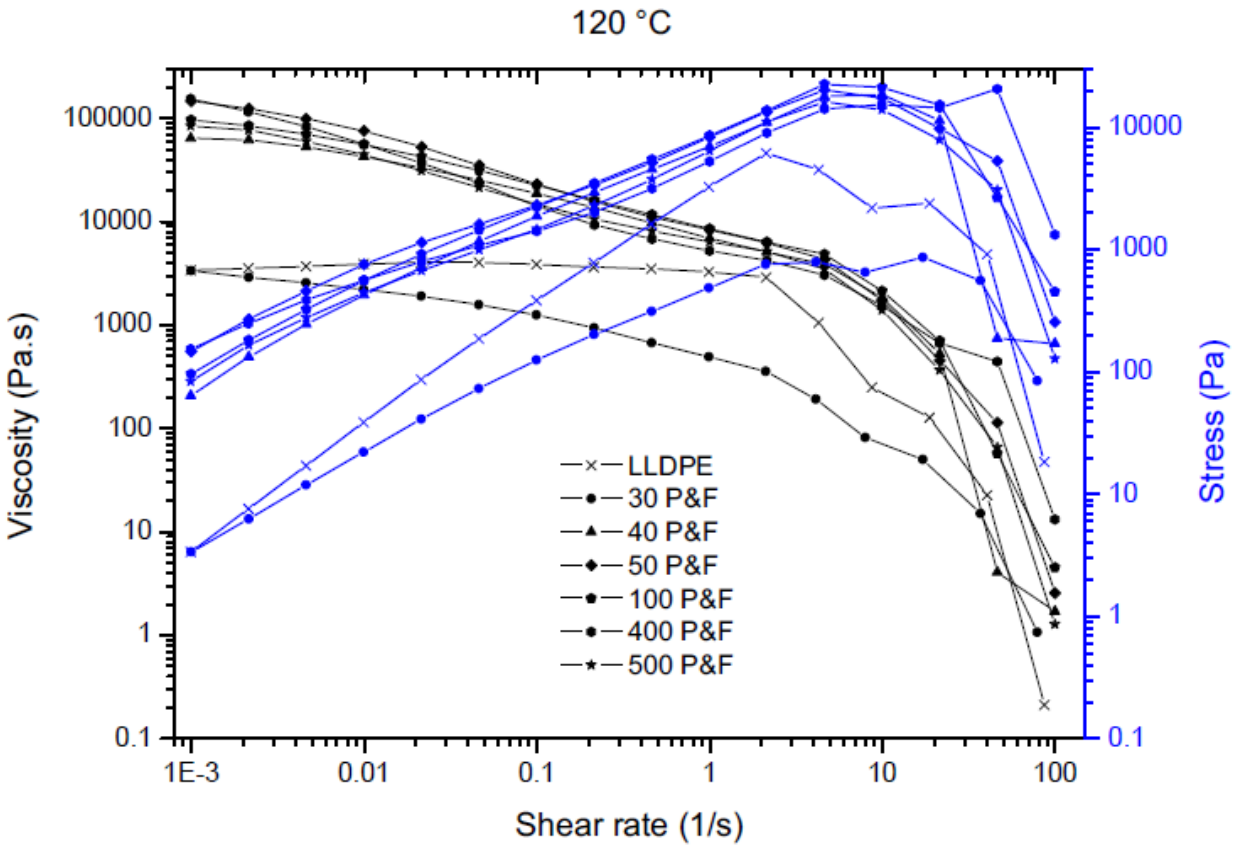

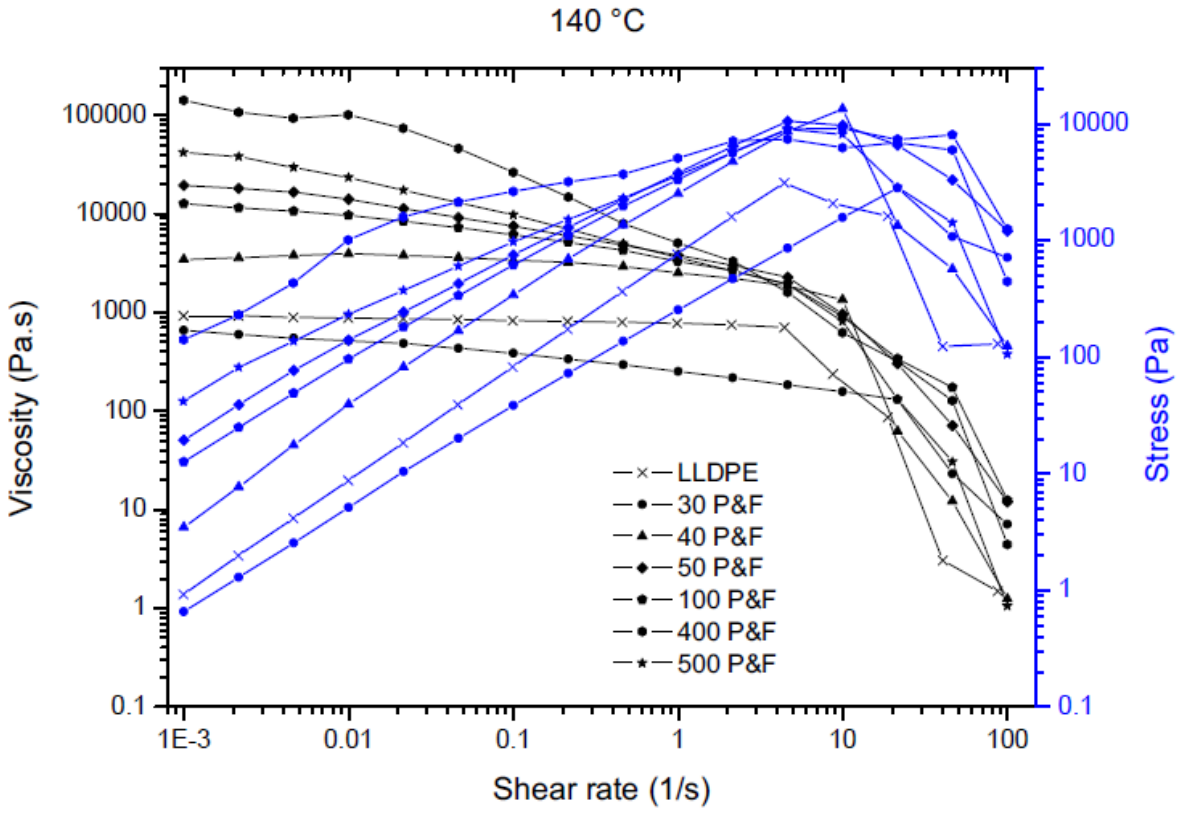
140 °C
Viscosity (Pa.s)
Stress (Pa)
Shear rate (1/s)
LLDPE
30 P&F
40 P&F
50 P&F
100 P&F
400 P&F
500 P&F

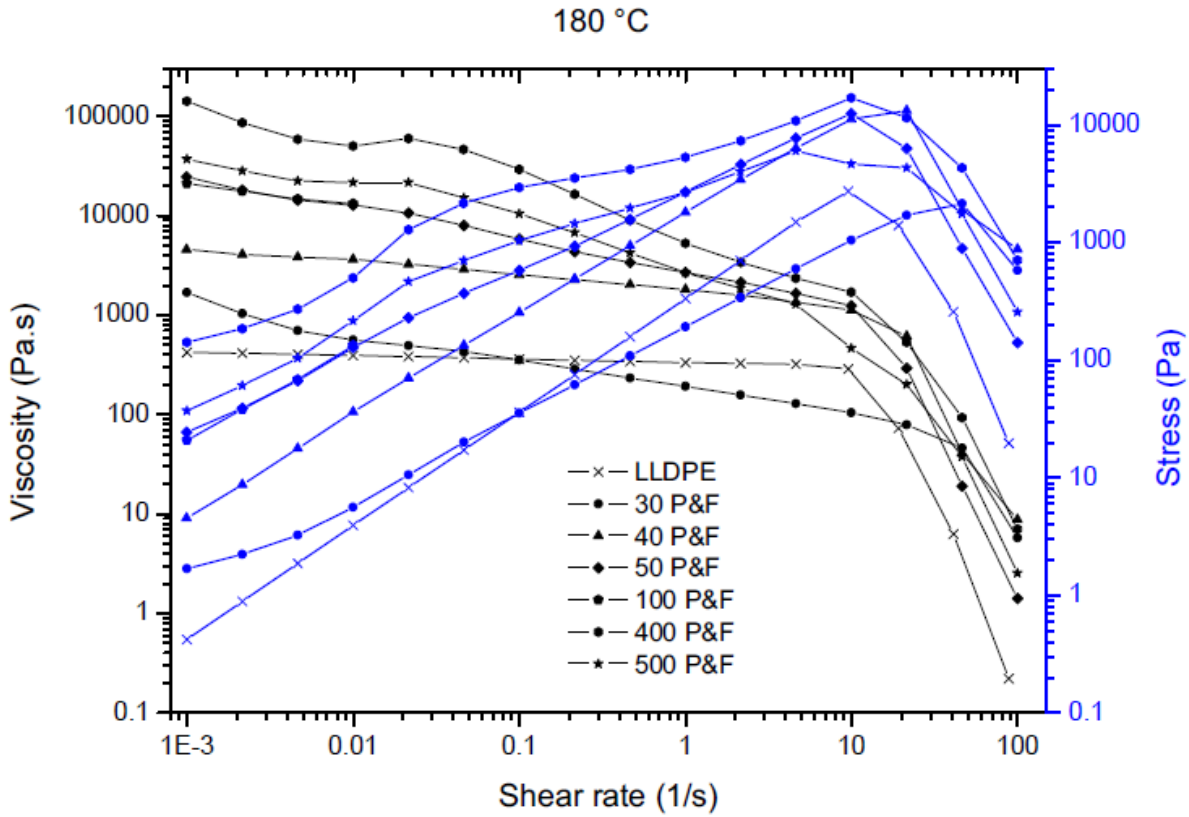
180 °C
Viscosity (Pa.s)
Stress (Pa)
Shear rate (1/s)
LLDPE
30 P&F
40 P&F
50 P&F
100 P&F
400 P&F
500 P&F

It is interesting to note that, for all the considered temperatures, the viscosity of the samples prepared with less than 40 P&F cycles is lower than the viscosity of neat LLDPE. Considering that microstructure of nanocomposites prepared with less than 50 P&F cycles presents agglomerates that are bigger than the dimensions of the initial GNP powder macro particles and that these samples also lost some GNP powder from their tensile fracture surfaces, it is fair to infer that such agglomerates act as a lubricant to the molten LLDPE matrix, lowering the viscosity of sample compared to that of neat LLDPE.

Samples prepared with more than 40 P&F cycles show increasing viscosity with the number of P&F cycles. When analysed at 120 °C, however, these samples do not show a remarkable increase of the viscosity with the number of P&F cycles as when they were analysed at higher temperatures do.

A common feature of the samples tasted at different temperatures is the decrease of the shear stress over a range of shear rates in which also the viscosity decreases. This can be explained by sample slippery on the rheometer walls.

Comparison with the literature

LLDPE usually found in literature has melt flow index (MI) of ~1 g/10min or less.[20–24] The MI of the LLDPE grade (Flexirene MS 20 A) used in our P&F project has a much higher MI: 26 g/10min. This must be due to a lower molecular weight of our polymer compared to the grades of LLDPE usually employed.

Consequently, the viscosity data found in literature (usually tested at 190 °C) are about 15-25 times higher than our LLDPE. However, a sample with MI of 50 g/min was reported to have a viscosity that was about half of the viscosity of our LLDPE.[23] Therefore, the viscosity measured for our LLDPE must be correct.

Moreover, literature data[20–24] show a decrease in the viscosity of about one order of magnitude within a rate of shear rate of 100-1000 1/s. Our LLDPE, conversely, shows this reduction over a range of 10-100 1/s (at 180 °C). This might be due both to a low mean molecular weight and to a wide molecular weight distribution of our LLDPE.

S.11 Model derivation

S.11.1 Estimation of the shear-rate during P&F

We approximate the flow during the P&F process as an axisymmetric squeeze flow between two parallel plates located at a distance 2*h*. The radius of the sample when the gap height is 2*h* is denoted by *R*.

In a cylindrical coordinate system with origin located at the midpoint between the plates, the radial velocity profile corresponding to a power-law fluid with constitutive equation $\tau_{rz} = m\left(-\frac{\partial v_r}{\partial r}\right)^n$ squeezed between two no-slip surfaces is[25]

$$v_r = \left(\frac{-\dot{h}r}{h}\right) B_n \left[1 - \left(\frac{z}{h}\right)^{1+1/n}\right]$$

Equation S6.

where $B_n = \frac{2n+1}{2n+2}$. The local shear rate is

$$\dot{\gamma} = \frac{\partial v_r}{\partial z} = \left(\frac{-\dot{h}r}{h^2}\right) B_n (1 + 1/n) \left(\frac{z}{h}\right)^{1/n}$$

Equation S7.

and the volume-averaged shear rate magnitude over the sample is

$$\langle\dot{\gamma}\rangle = \frac{1}{\pi R^2 h} \int_{r=0}^{R} \int_{z=0}^{h} |\dot{\gamma}|\, 2\pi r dr dz = \frac{2}{3} B_n \frac{\dot{h}R}{h^2}$$

Equation S8.

For $n > 0$, B_n varies weakly with n (for a shear thinning fluid, Bn varies from $B_n = 3/4$ for $n = 1$ to $B_n = 1/2$ for $n = 0$). In terms of orders of magnitude, we can thus write

$$\langle\dot{\gamma}\rangle = c_n \frac{\dot{h}R}{h^2}$$

Equation S9.

where c_n is a constant of order 1. In the case of slip surfaces, the flow is a uniform biaxial extensional flow and the average generalised shear rate is $\langle\dot{\gamma}\rangle = \sqrt{3}\frac{\dot{h}}{h}$.[26] Because $R/h \gg 1$, the average shear rate in the perfect slip case can be order of magnitude smaller than in the no-slip case.

In our experiment $|\dot{h}| \simeq 1.8$ mm/s, and *h* varies from 1 mm to 0.25 mm. During compression, the radius of the sample varies from 2 cm to 4 cm. In the case of slip surfaces, the average shear rate thus varies from 3 to 12 s^{-1} during compression. In the case of no-slip surfaces, the average shear rate varies from 36 s^{-1} to 1152 s^{-1}, where we have taken $c_n = 1$ for simplicity. The experimental case will likely be between the no-slip and the perfect slip case. We take $\langle\dot{\gamma}\rangle \sim 10$ s^{-1} and $\langle\dot{\gamma}\rangle \sim 1000$ s^{-1} as values representative of the initial and final stages of compression.

Fitting the LLDPE sample data for 10.7 wt.%, we obtain a power-law for the viscous stress $\tau \simeq \kappa\langle\dot{\gamma}\rangle^n$, where $\kappa \approx 500$ (in SI units) and $n \approx 0.75$. Using the reference values, the average stress is estimated to vary roughly between 3 KPa and 90 KPa during compression, depending on the adhesion of the polymer to the confining walls.

To evaluate whether exfoliation can take place, we need to compare the flow-induced stresses to the yield stress of the aggregate τ_y. For percolating suspensions, the following model has been recently proposed[27] that seems to fit well experimental data for graphene suspensions:

$$\sigma_y \simeq \frac{4}{3}\frac{\Gamma}{D_p}\phi_c^2 f(\phi/\phi_c)$$

Equation S10.

where ϕ is the volume fraction, ϕ_c is the volume fraction at the percolation threshold, $\Gamma \simeq 70$ mN/m is the graphene-graphene surface energy, D_p is the platelet diameter, and $f = \frac{(\phi/\phi_c - 1)^{2.5}}{(\phi/\phi_c + 1)^{0.5}}$. The percolation threshold can be estimated as $\phi_c \simeq 1.5t/D_p$,[27] where *t* is the thickness of each platelet. For $D_p/t = 26$,

close to the initial aspect-ratio of the microplates embedded into the polymer, we get $\phi_c \simeq 0.057$. For $D_p = 9.4$ µm, $\frac{\Gamma}{D_p}\phi_c^2 \simeq 2.4$ Pa. Accounting for the *f* factor, even assuming that the local volume fraction within a macro-aggregate is 10 times the percolation threshold ($\phi_c \simeq 0.57$), the aggregate yield stress is roughly 0.24 KPa, much less than the applied viscous stress. The formula above is probably not very accurate for dense macro-aggregates for which ϕ is close to 1. In this case, using basic fracture mechanics arguments, one may write the order of magnitude of the force required to break the contact between each platelet in the macro-aggregate as ΓD_p. The force acts over an area D_p^2, so the corresponding stress is of the order of $\sigma_y \sim \Gamma/D_p$, which is about 0.74 KPa. Also this estimate gives a yield stress value much smaller than the applied viscous stress.

S.11.2 Modelling of nanofiller dispersion and nanocomposite properties as a function of nanofiller dispersion level

The increase in interfacial area, *A(n)*, between GNP and LLDPE due to the distribution and dispersion after a particular interval of P&F cycles depends on the following aspects:

- Dimension of the considered interval of P&F cycles, *Δn*;
- Distribution rate, *I*, which is a constant that describes how the polymer melt can distribute the particles during the hot-pressing step;
- Difference between the total surface area of the particles, A_p, and the actual interfacial area with the matrix: $A_p - A(n)$. In fact, when all particles are in contact with the matrix ($A(n) = A_p$, *i.e.* perfect nanofiller dispersion) it is impossible to further increase the nanofiller-matrix interface, and distribution is the only phenomena that occurs in the P&F process.

In mathematical terms, this corresponds to the following equation:

$$\Delta A(n) = \Delta n \cdot I \cdot \left(A_p - A(n)\right)$$

Equation S11.

If $\Delta n \rightarrow 0$, the previous expression becomes a differential equation. Supposing that A_0 is the initial interfacial area at $n = 0$ P&F cycles, then a particular solution of this differential equation is the following:

$$A(n) = A_p - (A_p - A_0)e^{-I \cdot n}$$

Equation S12.

The total surface area A_p can be calculated from the specific surface area of GNP and the amount of GNP introduced in each sample. For example, the sample containing 4.8 vol.% of GNP was prepared with ~0.16 g, hence $A_p \approx 40000$ cm^2. The initial interfacial area A_0 can be easily estimated by measuring the

percentage of sample area covered by particles from the picture taken at 0 P&F cycles, and multiplying this by twice the total sample area (~100.5 cm^2). For the sample of 4.8 vol.% of GNP, $A_0 \approx 34$ cm^2.

For situations where the nanofiller is not well dispersed, *i.e.* until $A(n) \neq A_p$, it is not possible to completely use its reinforcing effect as predicted by the Halpin-Tsai model (reported in Section S.13.1). Indeed, the shear-lag theory of Cox states that there is load transfer from matrix to filler only when they are in perfect contact with each other. In other words, when the nanofiller is not well dispersed, its particles inside the agglomerates do not contribute to the properties of the nanocomposite. As a consequence, it is possible to exploit the volume fraction of the nanofiller only when it is completely in contact with the matrix, *i.e.* when $A(n) = A_p$. Thus, the effect of a not perfect dispersion is that the effective volume fraction, V_p^{eff}, is lower than the nominal one, V_p:

$$V_p^{eff} \equiv D \cdot V_p$$

Equation S13.

where D is a dispersion factor, which ranges from 0 (nanofiller and matrix are completely not in contact) to 1 (nanofiller perfectly dispersed and completely in contact with the matrix). How the dispersion factor varies with the interfacial area between nanofiller and matrix is challenging, and in first approximation, we could define the following definition:

$$D \approx \frac{A(n)}{A_p} = 1 - \frac{(A_p - A_0)e^{-I \cdot n}}{A_p}$$

Equation S14.

so when $A(n) = 0$ (no contact between nanofiller and matrix), then also D is zero, and when $A(n) = A_p$ (nanofiller perfectly dispersed and in contact with the matrix), than $D = 1$.

In general, any property as a function of nanofiller dispersion can be approximated by the following relationship:

$$P(D) \approx P_0 + (P_{th} - P_0) \cdot D$$

Equation S15.

where P is a particular property of the nanocomposite; P_0 is the property at D = 0; and P_{th} the expected value of the property when the nanofiller is perfectly dispersed (D = 1). For example, for the mechanical reinforcement $P = E_c/E_m = R$, P_0 = 1, and $P_{th}–P_0 = \eta \cdot (\zeta+1) \cdot V_p$ (after expansion of the Halpin-Tsai model in a first-order Maclaurin series). Similarly, for the yield stress $P = Y$, $P_0 = Y_m$ (yield stress of LLDPE), and $Y_{th}–Y_0 = Y_m \cdot (B_{Puk}–3.5) \cdot V_p$ (after expansion of the Pukanszky model, reported in Section S.13.2, in a first-order Maclaurin series).

By introducing the fitting parameters found for our mechanical reinforcement data (Section S.11.5) inside these relationships between Equation S15 and the Halpin-Tsai model, we can back-calculate a nanofiller aspect-ratio ξ of ~55. This result is close to ξ_{th} = 38 found from agglomerates aspect-ratio fit (Section S.11.5), and to ξ = 43 from the fitting of the reinforcement of nanocomposites containing different GNP loadings and prepared at 200 P&F cycles (see main article). Note that for the back-calculation we used a GNP and LLDPE moduli of 1 TPa and 140 MPa, respectively. However, the GNP modulus could be lower than 1 TPa (see Section S.3), but even using a modulus as low as ~65 GPa the final value of the aspect-ratio does not change significantly (~60 instead of ~55).

Similarly, by introducing the fitting parameters found for the yield data (Section S.11.5) inside the relationships between Equation S15 and the Pukanszky model, we can back-calculate an interaction parameter B_{Puk} of ~14. This result is similar to the value found from the fitting of yield stress of nanocomposites containing different GNP loadings and prepared at 200 P&F cycles (see main article).

Regarding the electrical conductivity, this property is strongly dependent on the distance between the particles of the nanofiller because the overall electrical conduction happens by electron tunnelling between the particles. Thus, the electrical conductivity could show a percolation behaviour, and its variation with nanofiller dispersion depends on the following aspects:

- Dimension of the considered interval of nanofiller dispersion, ΔD;
- a', which is a constant correlated to the velocity of the conductivity change with the inter-particle distance;
- Critical nanofiller dispersion, D_c, at which there is a quick change in electrical conductivity (for instance, from insulator to conductor), namely by the difference $D - D_c$;
- Asymptotic conductivity, σ_{th}, that is the theoretical conductivity when the nanofiller is perfectly dispersed (D=1) or when there is a drop-down of the percolation network due to inter-particle distances greater than the critical distance for electron tunnelling between particles. This corresponds to the difference $\sigma_{th} - \sigma$.

These aspects can be translated into a differential equation that can be solved to give the following relationship between conductivity and nanofiller dispersion:

$$\sigma(D) = \sigma_{th} + (\sigma_M - \sigma_{th}) \cdot e^{-a(D-D_c)^2}$$

Equation S16.

with D given by Equation S14. We believe that Equation S16 provides a more realistic description of the electrical conductivity than Equation S15.

S.11.3 Dispersion-factor for a melt-blending process

We note that Equation S14 can be adapted for the melt-blending process. In this case, *n* should be replaced by the processing time. The *I*-factor not only depends on types of nanofiller and polymer used, but also on shear rate and stress, and polymer viscosity. Moreover, the *I*-factor can be influenced by some aspects that can deteriorate both the polymer and the nanofiller, such as the delivered extrusion power, and processing time.

S.11.4 Dispersion-factor for a solution-mixing/casting process

Differently from our P&F process or melt-blending techniques, solution-mixing followed by solution casting is a bottom-up technique. Indeed, nanocomposites are formed by the joining of nanoparticles with polymers that happens directly at the nanoscale level when solvent is started being removed (solution casting), and grow up in volume with solvent evaporation. To understand how nanofiller can agglomerate during this process, we can refer to the work of Li and Kim,[28] who developed a model based on the average interparticle distance (IPD). Their model is used to quantify the critical nanofiller volume fraction for electrical percolation. Electrical percolation happens when the distance between the particles of nanofiller, d_{IP}, equals the critical length for electron hopping to occur from one particle to another one (and it is usually assumed around 10 nm).[28] Since the interparticle distance depends on the amount of nanofiller, Li and Kim could derive some expressions for the critical volume fractions for electrical percolation in nanocomposites containing different types of nanofillers and oriented in different distributions.

Similarly, we can find the critical volume fractions that start giving nanofiller agglomeration during solution casting. We just need to set the interparticle distance, d_{IP}, equal to zero. In this way, we can modify the expressions derived by Li and Kim to calculate the critical volume fraction for agglomeration in nanocomposites containing, for example, nanoplatelets organized in a planar distribution:

$$V_{p\_2D}^{c} = \frac{2\pi}{\xi}$$

Equation S17.

or nanoplatelets organized in a 3D random orientation:

$$V_{p\_3D}^{c} = \frac{27\pi}{4\xi}$$

Equation S18.

In both cases, the critical volume fractions depend on the aspect-ratio, ξ, of the nanoplatelets.

For nanofiller amounts higher than V_p^c, the nanoparticles are not completely in direct contact with the polymer matrix, so we can find a contact area, A_g, between them. In other words, A_g corresponds to the agglomeration contact area. The variation of this nanofiller agglomeration area may depend on the following factors:

- Variation in nanofiller volume fraction, ΔV_p;
- Difference between the total surface area of the nanoparticles, A_p, and the actual agglomeration contact area: $A_p - A_g$. In fact, when all nanoparticles are completely agglomerated, it is impossible to further increase the agglomeration contact area;
- *s*, which is a parameter that describes how fast the nanoparticles agglomerate. This parameter may be influenced by different aspects such as the nature of the nanoparticles (if nanoparticles interact with one another with strong Van der Waals forces, they are likely to agglomerate quickly); functionalization of nanoparticles or polymers (if nanoparticles can be easily bonded to the polymer matrix, it will be less likely that they agglomerate); and nanoparticle aspect-ratio (the higher the aspect-ratio, the more difficult is to control the configuration of the nanoparticles, and the more likely the nanoparticles crumple or fold).

These aspects can be translated into a differential equation that can be solved considering that when $V_p = V_p^c$, then A_g is zero:

$$A_g(V_p) = A_p - A_p e^{-s(V_p - V_p^c)}$$

Equation S19.

Eventually, considering that the nanofiller-polymer contact area is given by the difference $A_p - A_g$, we can derive the following dispersion factor for a solution-mixing/casting process:

$$\begin{cases} D_{s-m/c}(V_p) = 1 & \text{for } V_p \leq V_p^c \\ D_{s-m/c}(V_p) = e^{-s(V_p - V_p^c)} & \text{for } V_p > V_p^c \end{cases}$$

Equation S20.

By introducing this *D*-factor for the solution-mixing/casting process inside Equation S13, we can predict or describe the mechanical behaviour of casted nanocomposites affected by nanofiller agglomeration.

S.11.5 Model fitting of P&F data

We fitted the GNP agglomerate observations of Figure 1e and the mechanical properties of Figure 2b with Equation S15, and the electrical conductivities of Figure 2c with Equation S16 (all these figures are relative to the main article). In both cases, we used the P&F-related *D*-factor (Equation S14), thus we could find the distribution-rate *I* of the P&F process, useful to quantify the nanofiller dispersion level at different P&F cycles. Table S4 reports the fitting parameters for each property. As expected, the *I*-factor of the P&F process results to be independent of the analysed property. However, we decided to calculate a mean distribution-rate *I* of $(3.3 \pm 1.4)\cdot10^{-3}$ from the mechanical and electrical properties only, because the GNP agglomerate measurements could have been affected by some obvious problems of images resolution and operator-related errors.

Table S4. ***Fitting parameters of the properties of LLDPE + 4.8 vol.% GNP nanocomposites for our nanofiller dispersion models.***

Observable property, *P*	P&F-related dispersion model (Equation S14)	Predictive model of Equation S15		Predictive model of Equation S16		Adjusted R^2 of the fit
	I-factor	P_0	P_{th}	n_c *	a	
GM aspect-ratio, ξ	$5\cdot10^{-3}$	19.5	38	-	-	0.86
GM diameter, *d*	$29\cdot10^{-3}$	38 µm	4.9 µm	-	-	0.89
GM thickness, *t*	$27\cdot10^{-3}$	1.1 µm	112 nm	-	-	0.74
Reinforcement, *R*	$2.5\cdot10^{-3}$	1.02	2.8	-	-	0.79

Yield stress, *Y*	$3.9 \cdot 10^{-3}$	8.32 MPa	12.3 MPa	-	-	0.98
Stress at break, *B*	$5.5 \cdot 10^{-3}$	6.76 MPa	11.7 MPa	-	-	0.997
In-plane electrical conductivity, $\sigma_{i\text{-}p}$	$2.0 \cdot 10^{-3}$	-	-	96	114	0.80
Out-of-plane electrical conductivity, $\sigma_{o\text{-}o\text{-}p}$	$2.5 \cdot 10^{-3}$	-	-	97	84	0.64

* n_c is the critical number of P&F cycles, which is related to the critical nanofiller dispersion level, D_c, through Equation S14.

S.11.6 Another approach to estimate the distribution rates

The rate of a nanofiller distribution inside a certain matrix during the P&F dispersion process can be quickly calculated by using the initial nanofiller/matrix contact area (A_0), and the contact area after *n* P&F cycles (A_n):

$$I = \frac{1}{n} ln\left(\frac{A_p - A_0}{A_p - A_n}\right)$$

Equation S21.

The total nanofiller surface area (A_p) can be calculated using the specific surface area (*S*), and the amount *m* of nanofiller introduced inside a sample:

$$A_p = S \cdot m$$

Equation S22.

Both A_0 and A_n could be estimated by measuring the percentage, *C%*, of sample area covered by nanofiller from the optical pictures of the sample:

$$A_{0,n} = 2 \cdot sample\ area \cdot C\%$$

Equation S23.

Figure S11 shows the method used to calculate the sample area and *C%* from the optical pictures. A_n is more accurate if *C%* is measured at low (<5) P&F cycles, *i.e.* when the probability of having an overlapping of nanofiller agglomerates is low, thus A_n will not result underestimated.

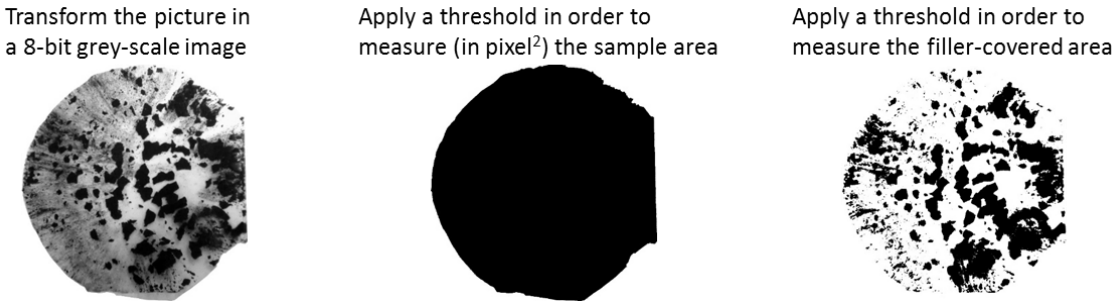

Figure S11. Method used to calculate the area of a sample, and its fraction covered by nanofiller.

With this method, we calculated a distribution-rate of $(3.5 \pm 2.0) \cdot 10^{-3}$ for GNP in LLDPE, by analysing the pictures taken during the first four P&F cycles. Despite this method may not be accurate, it still gives a good estimation of the distribution-rate. Indeed, the distribution-rate found from the fitting of the mechanical and electrical properties resulted quite similar, and equal to $(3.3 \pm 1.4) \cdot 10^{-3}$ (see Section S.10.3).

As the distribution-rate is important for the determination of the dispersion level of a nanofiller, in Table S5 we reported the distribution rates of different nanofiller/matrix systems.

Table S5. ***Distribution-rates for different nanofiller/matrix systems****.*

Matrix / Filler	LLDPE	HDPE	Phenoxy	PC	TPU
C-Therm 002 S = 25 m^2/g	$(3.5 \pm 2.0)\cdot10^{-3}$	$(9.3 \pm 1.5)\cdot10^{-3}$	$(7.4 \pm 1.0)\cdot10^{-3}$	$(2.3 \pm 1.0)\cdot10^{-3}$	$(5.43 \pm 0.23)\cdot10^{-3}$
xGnP 750 S = 100 m^2/g *	$(2.6 \pm 0.4)\cdot10^{-3}$	$(2.58 \pm 0.11)\cdot10^{-3}$	$(3.9 \pm 1.7)\cdot10^{-3}$	$(1.6 \pm 0.3)\cdot10^{-3}$	$(1.63 \pm 0.14)\cdot10^{-3}$
MMT (Cloisite 20A) $S \approx$ 800 m^2/g	$\geq7\cdot10^{-2}$	$\geq10\cdot10^{-2}$	$\geq2\cdot10^{-2}$		$\geq3\cdot10^{-2}$

* S calculated from XRD thickness: $S \approx 2/(d \cdot t_{XRD})$, where d is the density of graphite

Note that for the case of montmorillonite (MMT) nanocomposites, the MMT agglomerates disappear during the dispersion process, leaving the samples transparent. Therefore, we recorded the number n of P&F cycles needed to obtain a sample transparent to the naked eye and free of white agglomerates. We believe that when a sample does not show MMT agglomerates anymore, then the dispersion-factor must be at least 50%. Therefore, we estimated the distribution-rate with the following equation:

$$I = \frac{1}{n} ln\left(\frac{A_p - A_0}{0.5A_p}\right)$$

Equation S24.

The distribution-rates of MMT results to be much higher than GNP powders, and this might be due to the functionalization of the MMT used, or to a better nanofiller/matrix interaction that aid the dispersion process.

We tried to disperse also immiscible materials like magnetite nanoparticles and LLDPE, and we found that they can be well-mixed with a number of cycles higher than 200 (see figure below).

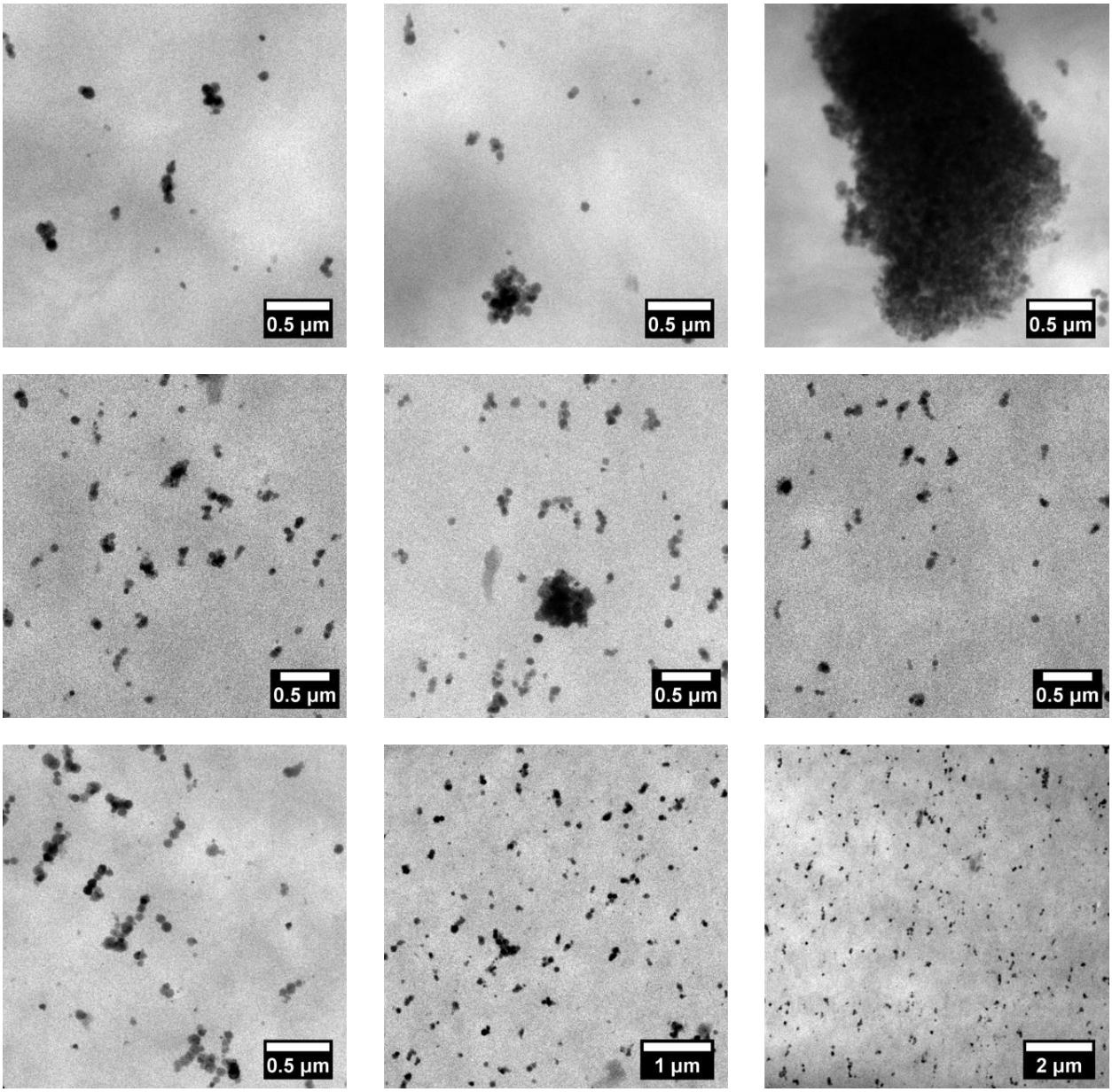

Figure S12. TEM images of LLDPE nanocomposites with 1.72 wt.% magnetite nanoparticles.

S.12 Potential applications

S.12.1 Joule-heating

Self-heating of nanocomposites was due to Joule effect when different electrical potentials were applied to the extremities of the samples (Figure S13). The inset pictures of the samples (Figure S13a, b, and c) were taken with a thermal camera, and show good thermal homogeneity reflecting an optimal microstructure. Note how the sample containing 7.4 vol.% GNP with a dispersion level of 48.2% (Figure S13b) heated up less than the sample containing 4.8 vol.% GNP (Figure S13a) because it's nanofiller dispersion state was grater, so less conductive paths were available for Joule heating.

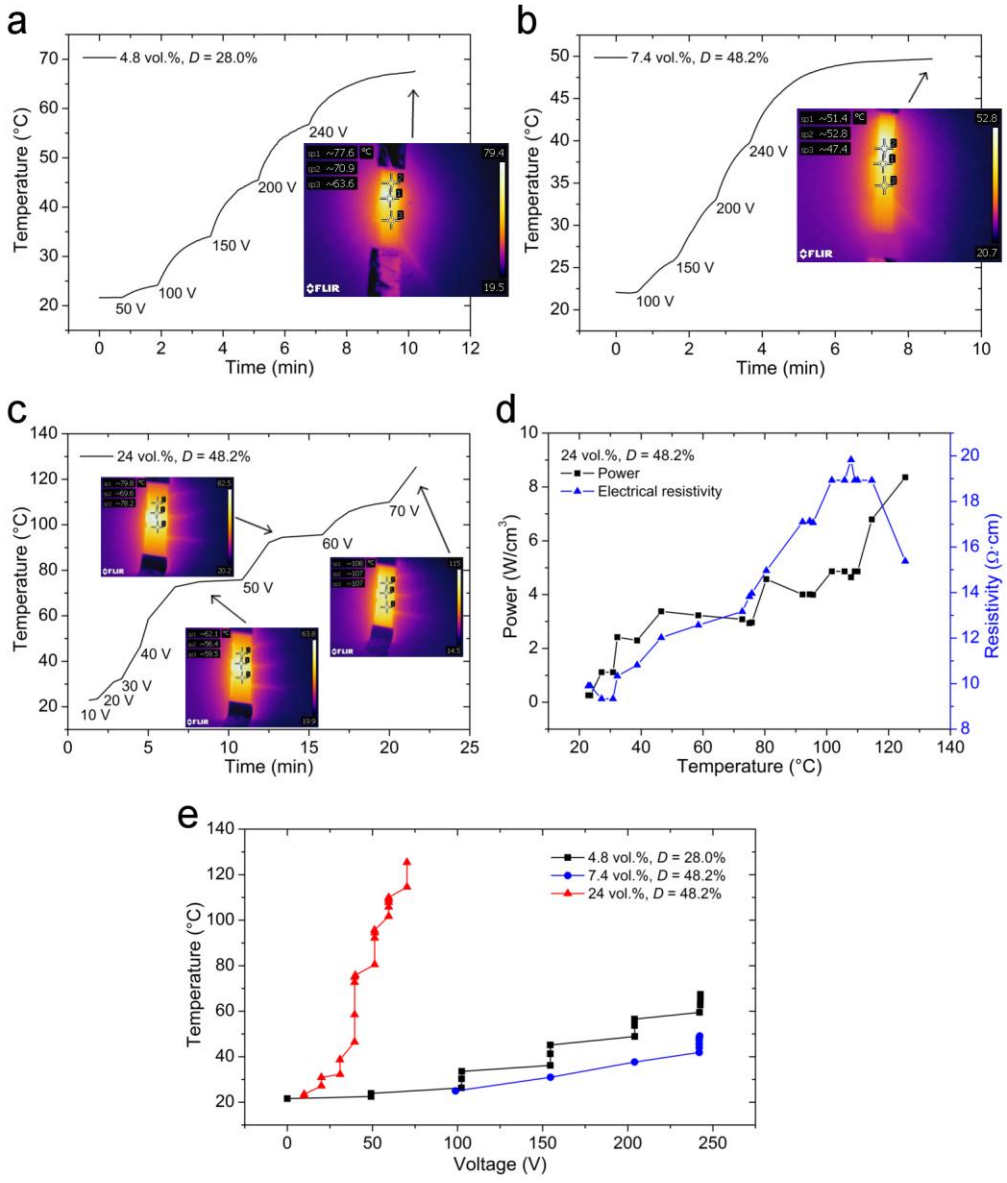

*Figure S13. Self-heating tests of LLDPE nanocomposites with different GNP loadings and dispersion levels. (**a**) Sample containing 4.8 vol.% GNP with a dispersion level of 28% reached a temperature of ~70 °C when 240 V of AC electrical potential difference was applied to its extremities. (**b**) Sample containing 7.4 vol.% GNP with a dispersion level of 48.2% reached only a temperature of ~50 °C after 240 V were applied. (**c**) Sample containing 24 vol.% GNP with a dispersion level of 48.2% reached the melting point after 70 V were applied; the power supplied to this sample and its resistivity increased with temperature (**d**). (**e**) Comparison of the self-heating behaviour of the tested samples as a function of the applied AC electrical potential difference.*

S.12.2 Strain sensing

Strain sensing during tensioning of nanocomposites (Figure S14) reveals that the variation of electrical resistance is much more evident for samples containing lower amounts of GNP. The sample containing 4.8 vol.% GNP with a dispersion level of 28% (close to the critical dispersion level D_c) presents a resistance variation similar to the sample of same composition but higher dispersion level (48.2%) only at high strains, when its conductivity approaches the theoretical one, σ_{th}. All nanocomposites presented several orders of magnitude variation in resistance before yielding (which occured around 15% of strain), demonstrating their suitability for structural health monitoring applications.

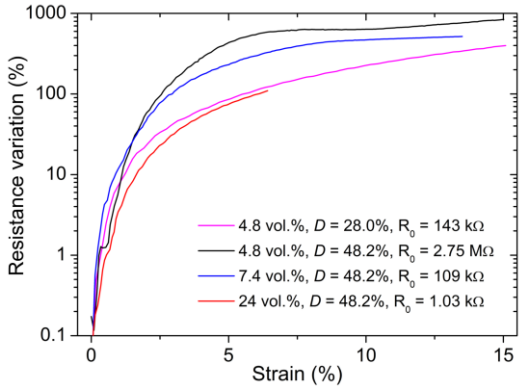

Figure S14. Variation of electrical resistance of LLDPE nanocomposites containing different GNP loadings and GNP dispersion states as a function of tensile strain.

S.12.3 Energy management

Polymer nanocomposites could be employed as high dielectric constant (high-k) and low loss materials for gate dielectrics, energy storage devices or electroactive materials.[29] Nanocarbon-polymer composites satisfy the synergistic requirements of high-k and limited loss just before reaching the percolation threshold. Above this point there is a huge increase in the dielectric loss, due to the ohmic electrical conduction of the percolated network. Figure 4a of the main paper shows how nanofiller agglomeration (samples containing 4.8 vol.% GNP with dispersion levels of 28% and 48.2%) reflects in conductive nanocomposites that are mainly resistive: the imaginary (Z'') *vs.* real impedance (Z') Nyquist plots of these samples show very small values of Z'' for a constant value of Z' (diverging slightly only at high frequencies due to the contact resistance). Higher dispersion levels and distribution of aligned GNP inside the dielectric LLDPE matrix result in nanocomposites with a capacitive behaviour (sample containing 4.8 vol.% GNP with a dispersion level 80.6%, see the C_3 || R_3 equivalent circuit, shown also in Figure S15b). This can be useful for high-k applications as they exhibit a high dielectric constant combined with a low dielectric loss.

Figure S15 shows the admittance magnitude of LLDPE nanocomposites containing 4.8 vol.% GNP with different nanofiller dispersion states. Admittance (Y), which is inversely proportional to impedance,[30] has been plotted to facilitate the relationship of AC-properties with DC-conductivity measurements. First, the pristine polymer that initially exhibits a purely capacitive behaviour (linear frequency-dependence, Figure S15a) is transformed into a conductive material (non-frequency dependant) when containing agglomerated states (*D*-factor of 28% and 48.2%) of 4.8 vol.% GNP. The different trends of |Y| along frequency support our previous observations of the electrical conductivity as a function of nanofiller dispersion (shown in Figure 2d of the main text), hence in accordance with the behaviour expected by Equation S16. Indeed, a slight agglomeration of nanofiller allows a conductive percolation network inside the material (admittance is predominantly real, Ohmic conduction), especially when is

close to the critical dispersion level, D_c, of Equation S16 (which corresponds to 25% for our nanocomposites containing 4.8 vol.% GNP). In such case, nanocomposites might be represented by the resistive equivalent circuit shown in Figure S15b (R_1 and R_2). However, when the nanofiller dispersion is increased, the nanocomposite conductivity decreases from high values (the highest is σ_M at the critical dispersion level) to lower values (approaching the theoretical conductivity, σ_{th}, expected by Equation S16 at high nanofiller dispersion states), because the percolation network becomes "disconnected" in many points. These "dead-ends" contribute to the formation of micro-capacitors at those conductive/dielectric/conductive regions of well-dispersed platelets with non-negligible interparticle gaps. Nanocomposites with such a microstructure containing highly dispersed GNP can be represented by a parallel R-C equivalent circuit, as depicted in Figure S15b (R_3 and C_3), and a frequency-dependent admittance is observed (see sample with *D*-factor = 80.6% in Figure S15a). Contrary to the common believe, this absence of percolation in nanocarbon/polymer nanocomposites can be also exploited for technological applications where dielectric materials with a high dielectric constant (real permittivity, ε') and a low dielectric loss (imaginary permittivity, ε'') are needed (*e.g.* gate dielectrics, energy storage devices, electroactive materials).[29] The real component of permittivity for dielectric/conductor nanocomposites is a measure of the migration and accumulation of charges at the dielectric/conductor interfaces (Maxwell–Wagner–Sillars polarization)[31], while the imaginary part is related to dielectric and conduction losses, associated to the material's ohmic resistance and the induced polarization, respectively. As seen from Figure S15c, the imaginary permittivity of the resistive samples (*D*-factors of 28% and 48.2%) is as high as 10^8 at low frequencies and decreases to 10^2 at 1 MHz. The sample with a high nanofiller dispersion of 80.6% has an imaginary permittivity that remains notably low, between 100 and 0.1 throughout the entire frequency window. Furthermore, this last sample shows a loss tangent ($\varepsilon''/\varepsilon'$) as low as ~0.1 (Figure S15d), in comparison with values above 10 for samples with lower nanofiller dispersions (*D*-factors of 28% and 48.2%). These results confirm that the electrical properties

of GNP-polymer nanocomposites can be tailored by the nanofiller dispersion state, exploiting the needs of a wide variety of conductive or insulating (capacitive) applications.

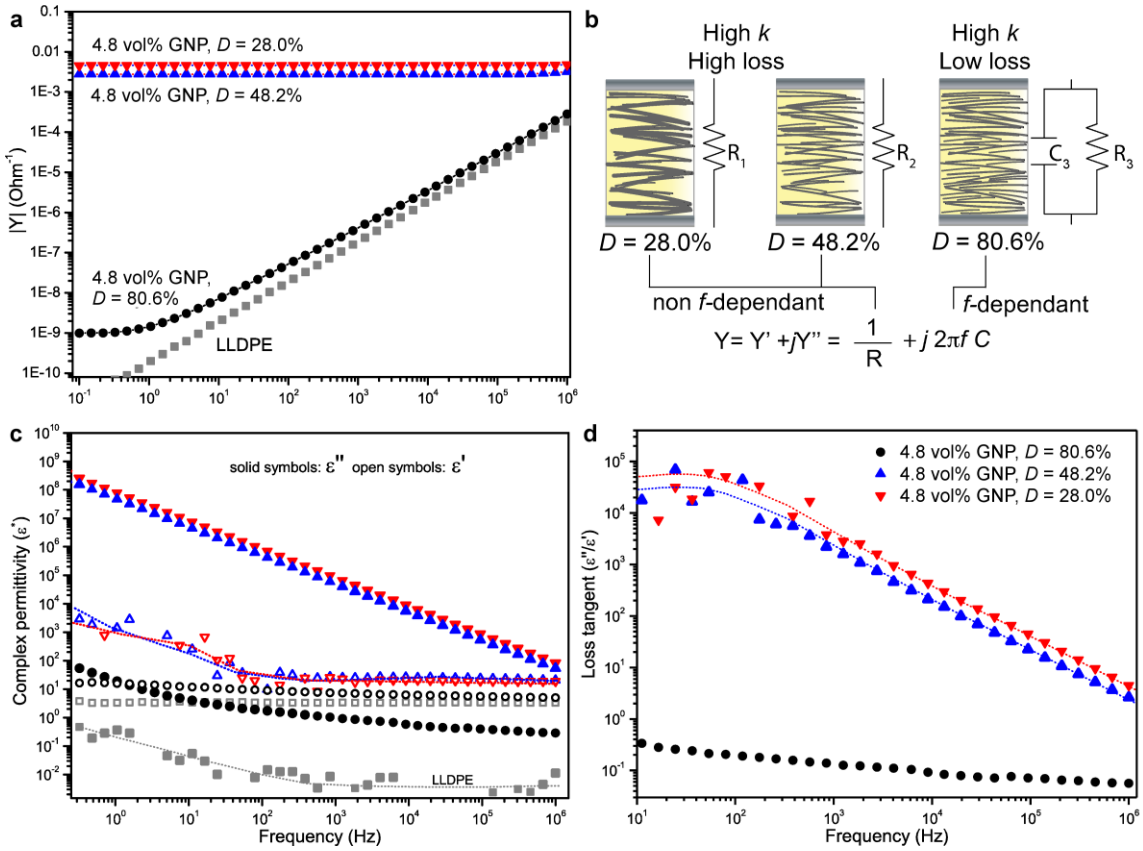

*Figure S15. Frequency sweep of: (**a**) admittance modulus (|Y|), (**c**) complex permittivity, and (**d**) loss tangent for LLDPE nanocomposites containing 4.8 vol.% GNP with different nanofiller dispersion levels. (**b**) Draw that summarizes the observed behaviours: while a nanofiller dispersion close to the critical dispersion level, D_c (≈ 25% for these samples), of Equation S16 makes the nanocomposites conductive (resistive, R_1 and R_2), high dielectric constant (ε′, high-k) and low loss tangent (ε′′/ε′) nanocomposites can be addressed only if the nanofiller dispersion state is optimized (close to 100%).*

S.12.4 MMT nanocomposites

Nanocomposites of LLDPE and montmorillonite were prepared introducing a high amount of Cloisite 20A between two polymeric films. The sample was characterised after 50 P&F cycles, because at this number of cycles should correspond a MMT dispersion of ~99% considering the distribution-rate found in Section S.10.4. Thermal gravimetric analysis (TGA) revealed a MMT content of ~74 wt.%. Tensile tests revealed a Young's modulus of ~1.8 GPa, a strength of ~12.5 MPa, and a strain at break of ~1%.

We also prepared a reference sample with a mini-extruder. We managed to introduce ~50 wt.% MMT in several steps, differently from the P&F sample in which LLDPE and MMT were mixed in one-go. TGA revealed a final MMT content of ~48 wt.%. The lower concentration of MMT of this sample compared to the P&F one reflected on higher strain at break (~12%), but lower stiffness (~320 MPa) and strength (~9.3 MPa).

In order to assess our nanocomposites, Table S6 reports the mechanical reinforcement found in literature for MMT nanocomposites with non-elastomeric matrices. Our P&F sample is the highest loaded and reinforced sample ever reported for nanocomposites prepared by melt-blending. Our other sample prepared with the mini-extruder has a mechanical reinforcement similar to those found in literature for melt-blended nanocomposites. Only bottom-up techniques, such as solution processing and layer-by-layer, can reach the same loading and mechanical reinforcement of our P&F sample. The box chart of Figure 4d in the main text is based on the data of Table S6.

Table S6. ***Mechanical reinforcement found in literature for MMT nanocomposites prepared by melt processing, solution processing, or layer-by-layer****.*

Processing technique	Matrix	MMT content (wt.%)	Mechanical reinforcement (E_c/E_m)	Reference
Melt blending	PVC	0.5 1 3 5	1.01 1.01 1.06 1.04	32
Solution processing	PLA	2 4 6 8	1.22 1.36 1.33 1.31	33
Melt blending	PA6	1.5 2.9 4.6 6.6	1.26 1.53 1.69 1.85	34
Melt blending	PA6	2 4 6.5	1.30 1.50 1.73	34
Solution processing	PET	1 2 3	1.30 1.49 1.85	35
Solution processing	PVA	2 4 6 10	1.80 3.10 2.75 3.40	36
Solution processing	PS	3.6 5.6 7.6	1.15 1.31 1.59	37
Melt blending	PBS	1.5 2.5 4 5.5	1.19 1.42 1.80 3.46	38
Melt blending	LLDPE	0.8 2.5 4.6 6.9	1.39 1.80 2.52 2.99	39
Melt blending	PLA	1.2 3 4	1.46 1.49 1.65	40
Solution processing	PS	5 10 20 30	1.07 1.57 2.18 1.51	41

Solution processing	Chitosan	2.5 5 10	1.09 1.16 1.26	42
Solution processing	Polyester	3 5 7 10	1.12 1.22 1.18 1.32	43
Melt blending	PLA	2.5 5 7.5	1.17 1.32 1.50	44
Solution processing	PLA	2 4 6 8	1.22 1.37 1.32 1.31	45
Solution processing	PLA	2 4 6 8	1.21 1.29 1.49 3.04	45
Melt blending	LDPE	3 6	1.02 1.03	46
Melt blending	PA6	2.7 4.9	1.45 1.66	47
Solution processing	Cellulose	1 5 10 25 50	1.01 1.56 1.55 1.69 1.67	48
Solution processing	PEO	76 85	6.25 15.9	49
Solution processing	Cellulose	60 83	3.70 5.80	49
LbL	PVA	70	7.64	50
LbL	PVA-GA	70	53.0	50
LbL	PDDA	80	68.7	51
LbL	Chitosan	80	3.21	52
LbL	PVA	70 70 70	7.64 24.1 34.1	53
LbL	PAA	70	6.14	54
LbL	PVA	55	5.89	55
LbL	PVA	96 97 98 99	2.22 4.88 24.8 18.8	56
LbL	PVP	95	3.80	57

S.13 Classical composite theories

S.13.1 Halpin-Tsai model

The mechanical reinforcement due to a nanofiller – which can be defined as the ratio between the Young's moduli of the nanocomposite (E_c) and the neat polymer (E_m) – depends on its aspect-ratio ξ (the ratio between its diameter and thickness, assuming a disc-like platelet), volume fraction V_p, and Young's modulus of the filler (E_p). Therefore, assuming an in-plane nanofiller orientation, it is possible to predict the mechanical reinforcement along the plane of a nanocomposite by using the Halpin-Tsai equations:[58,59]

$$\frac{E_c}{E_m} = \frac{1 + \zeta \eta V_p}{1 - \eta V_p}$$

Equation S25.

with

$$\eta = \frac{\frac{E_p}{E_m} - 1}{\frac{E_p}{E_m} + \zeta}$$

Equation S26.

where ζ is a shape-factor, which depends on the nanofiller aspect-ratio:[60]

$$\zeta = \frac{2}{3}\xi$$

Equation S27.

Note that if $\xi \rightarrow \infty$, the Halpin-Tsai model equals the (upper bound) rule of mixtures (RoM), whereas if $\xi \rightarrow 0$, it equals the (lower bound) inverse rule of mixtures (IRoM).

S.13.2 Pukanszky model

The size of a nanofiller is connected to its specific surface area, which can influence the yield stress Y_c of a nanocomposite. This is taken into account by the interaction parameter B_{Puk} of the Pukanszky model:[61]

$$Y_c = Y_m \frac{1 - V_p}{1 + 2.5V_p} e^{B_{Puk} \cdot V_p}$$

Equation S28.

where Y_m is the yield stress of the polymer matrix. Moreover, the stronger the interaction between nanofiller and matrix, the higher the parameter B_{Puk}, resulting in higher yield stress values.

S.14 References

(1) Kuila, T.; Bose, S.; Mishra, A. K.; Khanra, P.; Kim, N. H.; Lee, J. H. Effect of Functionalized Graphene on the Physical Properties of Linear Low Density Polyethylene Nanocomposites. *Polym. Test.* **2012**, *31*, 31–38

(2) Kundu, P. P.; Biswas, J.; Kim, H.; Choe, S. Influence of Film Preparation Procedures on the Crystallinity, Morphology and Mechanical Properties of LLDPE Films. *Eur. Polym. J.* **2003**, *39*, 1585–1593

(3) Hermans, P. H.; Weidinger, A. On the Determination of the Crystalline Fraction of Polyethylenes from X-Ray Diffraction. *Makromol. Chem.* **1961**, *44*, 24–36

(4) Oskouyi, A. B.; Sundararaj, U.; Mertiny, P. Current-Voltage Characteristics of Nanoplatelet-Based Conductive Nanocomposites. *Nanoscale Res. Lett.* **2014**, *9*, 1–8

(5) Nezakati, T.; Tan, A.; Seifalian, A. M. Enhancing the Electrical Conductivity of a Hybrid POSS–PCL/Graphene Nanocomposite Polymer. *J. Colloid Interface Sci.* **2014**, *435*, 145–155

(6) Kouroupis-Agalou, K.; Liscio, A.; Treossi, E.; Ortolani, L.; Morandi, V.; Pugno, N. M.; Palermo, V. Fragmentation and Exfoliation of 2-Dimensional Materials: A Statistical Approach. *Nanoscale* **2014**, *6*, 5926

(7) Krzesińska, M.; Celzard, A.; Marêché, J. F.; Puricelli, S. Elastic Properties of Anisotropic Monolithic Samples of Compressed Expanded Graphite Studied with Ultrasounds. *J. Mater. Res.* **2001**, *16*, 606–614

(8) Sun, G.; Li, X.; Qu, Y.; Wang, X.; Yan, H.; Zhang, Y. Preparation and Characterization of Graphite Nanosheets from Detonation Technique. *Mater. Lett.* **2008**, *62*, 703–706

(9) Howe, J. Y.; Cavin, B. O.; Drakeford, A. E.; Peascoe, R. A.; Zontek, T. L.; Miller, D. J. Influence of Bulk Graphite Thickness on the Accuracy of X-Ray Diffraction Measurement. In *Carbon 2007*; Seattle, Washington, USA, 2007

(10) Chung, D. D. L. Review Graphite. *J. Mater. Sci.* **2002**, *37*, 1475–1489

(11) Blanton, T. N.; Majumdar, D. X-Ray Diffraction Characterization of Polymer Intercalated Graphite Oxide. *Powder Diffr.* **2012**, *27*, 104–107
(12) Gong, L.; Young, R. J.; Kinloch, I. A.; Riaz, I.; Jalil, R.; Novoselov, K. S. Optimizing the Reinforcement of Polymer-Based Nanocomposites by Graphene. *ACS Nano* **2012**, *6*, 2086–2095
(13) Chen, W.; Qu, B. LLDPE/ZnAl LDH-Exfoliated Nanocomposites: Effects of Nanolayers on Thermal and Mechanical Properties. *J. Mater. Chem.* **2004**, *14*, 1705
(14) Wirsén, A.; Lindberg, K. T.; Albertsson, A.-C. Graft Polymerization of Acrylamide onto Linear Low-Density Polyethylene Film by Electron Beam Pre-Irradiation in Air or Argon: 3. Morphology. *Polymer* **1996**, *37*, 761–769
(15) Zhang, K.; Zhang, Y.; Wang, S. Enhancing Thermoelectric Properties of Organic Composites through Hierarchical Nanostructures. *Sci. Rep.* **2013**, *3*
(16) Seung Hun, H.; Hae-Mi, J.; Sung-Ho, C. X-Ray Diffraction Patterns of Thermally-Reduced Graphenes. *J. Korean Phys. Soc.* **2010**, *57*, 1649
(17) Vasileiou, A. A.; Kontopoulou, M.; Docoslis, A. A Noncovalent Compatibilization Approach to Improve the Filler Dispersion and Properties of Polyethylene/Graphene Composites. *ACS Appl. Mater. Interfaces* **2014**, *6*, 1916–1925
(18) Kim, H.; Kobayashi, S.; AbdurRahim, M. A.; Zhang, M. J.; Khusainova, A.; Hillmyer, M. A.; Abdala, A. A.; Macosko, C. W. Graphene/Polyethylene Nanocomposites: Effect of Polyethylene Functionalization and Blending Methods. *Polymer* **2011**, *52*, 1837–1846
(19) Carotenuto, G.; De Nicola, S.; Palomba, M.; Pullini, D.; Horsewell, A.; Hansen, T. W.; Nicolais, L. Mechanical Properties of Low-Density Polyethylene Filled by Graphite Nanoplatelets. *Nanotechnology* **2012**, *23*, 485705
(20) Constantin, D. Linear-low-density Polyethylene Melt Rheology: Extensibility and Extrusion Defects. *Polym. Eng. Sci.* **1984**, *24*, 268–274
(21) Dartora, P. C.; Santana, R. M. C.; Moreira, A. C. F.; Dartora, P. C.; Santana, R. M. C.; Moreira, A. C. F. The Influence of Long Chain Branches of LLDPE on Processability and Physical Properties. *Polímeros* **2015**, *25*, 531–539
(22) Mackley, M. R.; Spitteler, P. H. J. Experimental Observations on the Pressure-Dependent Polymer Melt Rheology of Linear Low Density Polyethylene, Using a Multi-Pass Rheometer. *Rheol. Acta* **1996**, *35*, 202–209
(23) Liang, J. Z.; Ness, J. N. Studies on Melt Flow Properties of Low Density and Linear Low Density Polyethylene Blends in Capillary Extrusion. *Polym. Test.* **1997**, *16*, 173–184
(24) Steffl, T. Rheological and Film Blowing Properties of Various Low Density Polyethylenes and Their Blends, Erlangen-Nürnberg, Univ., Diss., 2004
(25) Leider, P. J.; Bird, R. B. Squeezing Flow between Parallel Disks. I. Theoretical Analysis. *Ind. Eng. Chem. Fundam.* **1974**, *13*, 336–341
(26) Engmann, J.; Servais, C.; Burbidge, A. S. Squeeze Flow Theory and Applications to Rheometry: A Review. *J. Non-Newton. Fluid Mech.* **2005**, *132*, 1–27
(27) Barwich, S.; Coleman, J. N.; Möbius, M. E. Yielding and Flow of Highly Concentrated, Few-Layer Graphene Suspensions. *Soft Matter* **2015**, *11*, 3159–3164
(28) Li, J.; Kim, J.-K. Percolation Threshold of Conducting Polymer Composites Containing 3D Randomly Distributed Graphite Nanoplatelets. *Compos. Sci. Technol.* **2007**, *67*, 2114–2120
(29) Yuan, J.; Luna, A.; Neri, W.; Zakri, C.; Schilling, T.; Colin, A.; Poulin, P. Graphene Liquid Crystal Retarded Percolation for New High-k Materials. *Nat. Commun.* **2015**, *6*, 8700
(30) Sandler, J.; Shaffer, M. S. P.; Prasse, T.; Bauhofer, W.; Schulte, K.; Windle, A. H. Development of a Dispersion Process for Carbon Nanotubes in an Epoxy Matrix and the Resulting Electrical Properties. *Polymer* **1999**, *40*, 5967–5971

(31) Dang, Z.-M.; Yuan, J.-K.; Yao, S.-H.; Liao, R.-J. Flexible Nanodielectric Materials with High Permittivity for Power Energy Storage. *Adv. Mater.* **2013**, *25*, 6334–6365
(32) Wan, C.; Qiao, X.; Zhang, Y.; Zhang, Y. Effect of Different Clay Treatment on Morphology and Mechanical Properties of PVC-Clay Nanocomposites. *Polym. Test.* **2003**, *22*, 453–461
(33) Chang, J.-H.; An, Y. U.; Sur, G. S. Poly(Lactic Acid) Nanocomposites with Various Organoclays. I. Thermomechanical Properties, Morphology, and Gas Permeability. *J. Polym. Sci. Part B Polym. Phys.* **2003**, *41*, 94–103
(34) Shah, R. K.; Paul, D. R. Nylon 6 Nanocomposites Prepared by a Melt Mixing Masterbatch Process. *Polymer* **2004**, *45*, 2991–3000
(35) Chang, J.-H.; Kim, S. J.; Joo, Y. L.; Im, S. Poly(Ethylene Terephthalate) Nanocomposites by in Situ Interlayer Polymerization: The Thermo-Mechanical Properties and Morphology of the Hybrid Fibers. *Polymer* **2004**, *45*, 919–926
(36) Strawhecker, K. E.; Manias, E. Structure and Properties of Poly(Vinyl Alcohol)/Na^+ Montmorillonite Nanocomposites. *Chem. Mater.* **2000**, *12*, 2943–2949
(37) Fu, X.; Qutubuddin, S. Polymer–Clay Nanocomposites: Exfoliation of Organophilic Montmorillonite Nanolayers in Polystyrene. *Polymer* **2001**, *42*, 807–813
(38) Sinha Ray, S.; Okamoto, K.; Okamoto, M. Structure−Property Relationship in Biodegradable Poly(Butylene Succinate)/Layered Silicate Nanocomposites. *Macromolecules* **2003**, *36*, 2355–2367
(39) Hotta, S.; Paul, D. R. Nanocomposites Formed from Linear Low Density Polyethylene and Organoclays. *Polymer* **2004**, *45*, 7639–7654
(40) Maiti, P.; Yamada, K.; Okamoto, M.; Ueda, K.; Okamoto, K. New Polylactide/Layered Silicate Nanocomposites: Role of Organoclays. *Chem. Mater.* **2002**, *14*, 4654–4661
(41) Noh, M. W.; Lee, D. C. Synthesis and Characterization of PS-Clay Nanocomposite by Emulsion Polymerization. *Polym. Bull.* **1999**, *42*, 619–626
(42) Wang, S. F.; Shen, L.; Tong, Y. J.; Chen, L.; Phang, I. Y.; Lim, P. Q.; Liu, T. X. Biopolymer Chitosan/Montmorillonite Nanocomposites: Preparation and Characterization. *Polym. Degrad. Stab.* **2005**, *90*, 123–131
(43) Kornmann, X.; Berglund, L. A.; Sterte, J.; Giannelis, E. P. Nanocomposites Based on Montmorillonite and Unsaturated Polyester. *Polym. Eng. Sci.* **1998**, *38*, 1351–1358
(44) Jiang, L.; Zhang, J.; Wolcott, M. P. Comparison of Polylactide/Nano-Sized Calcium Carbonate and Polylactide/Montmorillonite Composites: Reinforcing Effects and Toughening Mechanisms. *Polymer* **2007**, *48*, 7632–7644
(45) Chang, J.-H.; An, Y. U.; Cho, D.; Giannelis, E. P. Poly(Lactic Acid) Nanocomposites: Comparison of Their Properties with Montmorillonite and Synthetic Mica (II). *Polymer* **2003**, *44*, 3715–3720
(46) Morawiec, J.; Pawlak, A.; Slouf, M.; Galeski, A.; Piorkowska, E.; Krasnikowa, N. Preparation and Properties of Compatibilized LDPE/Organo-Modified Montmorillonite Nanocomposites. *Eur. Polym. J.* **2005**, *41*, 1115–1122
(47) Chavarria, F.; Paul, D. R. Comparison of Nanocomposites Based on Nylon 6 and Nylon 66. *Polymer* **2004**, *45*, 8501–8515
(48) Wu, C.-N.; Saito, T.; Fujisawa, S.; Fukuzumi, H.; Isogai, A. Ultrastrong and High Gas-Barrier Nanocellulose/Clay-Layered Composites. *Biomacromolecules* **2012**, *13*, 1927–1932
(49) Sehaqui, H.; Kochumalayil, J.; Liu, A.; Zimmermann, T.; Berglund, L. A. Multifunctional Nanoclay Hybrids of High Toughness, Thermal, and Barrier Performances. *ACS Appl. Mater. Interfaces* **2013**, *5*, 7613–7620
(50) Podsiadlo, P.; Kaushik, A. K.; Arruda, E. M.; Waas, A. M.; Shim, B. S.; Xu, J.; Nandivada, H.; Pumplin, B. G.; Lahann, J.; Ramamoorthy, A.; Kotov, N. A. Ultrastrong and Stiff Layered Polymer Nanocomposites. *Science* **2007**, *318*, 80–83

(51) Tang, Z.; Kotov, N. A.; Magonov, S.; Ozturk, B. Nanostructured Artificial Nacre. *Nat. Mater.* **2003**, *2*, 413–418
(52) Podsiadlo, P.; Tang, Z.; Shim, B. S.; Kotov, N. A. Counterintuitive Effect of Molecular Strength and Role of Molecular Rigidity on Mechanical Properties of Layer-by-Layer Assembled Nanocomposites. *Nano Lett.* **2007**, *7*, 1224–1231
(53) Podsiadlo, P.; Kaushik, A. K.; Shim, B. S.; Agarwal, A.; Tang, Z.; Waas, A. M.; Arruda, E. M.; Kotov, N. A. Can Nature's Design Be Improved Upon? High Strength, Transparent Nacre-Like Nanocomposites with Double Network of Sacrificial Cross Links †. *J. Phys. Chem. B* **2008**, *112*, 14359–14363
(54) Huang, G.; Ge, C.; He, B. Preparation, Characterization and Properties of Amino-Functionalized Montmorillonite and Composite Layer-by-Layer Assembly with Inorganic Nanosheets. *Appl. Surf. Sci.* **2011**, *257*, 7123–7128
(55) Gaidukov, S.; Danilenko, I.; Gaidukova, G. Characterization of Strong and Crystalline Polyvinyl Alcohol/Montmorillonite Films Prepared by Layer-by-Layer Deposition Method. *Int. J. Polym. Sci.* **2015**, *2015*, 1–8
(56) Shu, Y.; Yin, P.; Liang, B.; Wang, H.; Guo, L. Bioinspired Design and Assembly of Layered Double Hydroxide/Poly(Vinyl Alcohol) Film with High Mechanical Performance. *ACS Appl. Mater. Interfaces* **2014**, 140825162306007
(57) Finnemore, A.; Cunha, P.; Shean, T.; Vignolini, S.; Guldin, S.; Oyen, M.; Steiner, U. Biomimetic Layer-by-Layer Assembly of Artificial Nacre. *Nat. Commun.* **2012**, *3*, 966
(58) Affdl, J. C. H.; Kardos, J. L. The Halpin-Tsai Equations: A Review. *Polym. Eng. Sci.* **1976**, *16*, 344–352
(59) Halpin, J. C.; Thomas, R. L. Ribbon Reinforcement of Composites. *J. Compos. Mater.* **1968**, *2*, 488–497
(60) Van Es, M. A.; Van Turnhout, J. Polymer-Clay Nanocomposites: The Importance of Particle Dimensions. Ph.D. Thesis, Delft University of Technology, 2001
(61) Turcsányi, B.; Pukánszky, B.; Tüdős, F. Composition Dependence of Tensile Yield Stress in Filled Polymers. *J. Mater. Sci. Lett.* **1988**, *7*, 160–162